International Journal of Heat and Mass Transfer 149 (2020) 119158

Contents lists available at ScienceDirect

International Journal of Heat and Mass Transfer

journal homepage: www.elsevier.com/locate/hmt

Computational and experimental investigation of condensation flow patterns and heat transfer in parallel rectangular micro-channels

Yuchuan Lei[a], Issam Mudawar[b,*], Zhenqian Chen[a]

[a] School of Energy & Environment, Southeast University, Nanjing, Jiangsu, PR China
[b] Purdue University Boiling and Two-Phase Flow Laboratory (PU-BTPFL), School of Mechanical Engineering, Purdue University, 585 Purdue Mall, West Lafayette, IN 47907, USA

ARTICLE INFO

Article history:
Received 30 August 2019
Revised 1 December 2019
Accepted 1 December 2019
Available online 15 December 2019

Keywords:
Condensation
Two-phase flow patterns
CFD
Micro-channels

ABSTRACT

This study explores experimentally and computationally fluid flow and heat transfer characteristics of FC-72 condensation along a cooling module containing multiple 1 mm × 1 mm square channels. The module is cooled along its underside by a counterflow of water. The computational portion of the study adopts the VOF method and Lee interfacial phase change model, and is executed using ANSYS FLUENT. Computed are dominant flow patterns as well as spatial variations of both bottom wall temperature and fluid temperature for FC-72 mass velocities ranging from 68 to 367 kg/m^{2}s. The computed flow patterns show good agreement with those captured experimentally using high-speed video. Captured correctly are dominant smooth-annular, wavy-annular, transition, slug, bubbly, and pure liquid flow patterns. And predicted variations of wall temperature show good agreement between computational results, with average deviation ranging from 1.46% to 6.81%. The computational method is capable of predicting fluid temperature, which cannot be measured experimentally in a small channel. Detailed spatial variations of fluid temperature are provided both perpendicular to the bottom wall and along the channel. These variations show close correspondence with axial spans of the dominant flow patterns.

1. Introduction

1.1. Significance of two-phase thermal management

During the mid-1980s, rapid escalation of heat dissipation from computer electronics prompted system developers to transition from air-cooling schemes to those employing single-phase liquid cooling. However, continued miniaturization of electronic components in devices continued to compound the heat dissipation problem. And in ensuing decades, this was no longer limited to computer electronics, but to many other applications, including hybrid vehicle power electronics, avionics, lasers, and radar [1–3]. Another important application is thermal control systems essential to next generation space vehicles [4–6]. Currently, heat dissipation demands have already surpassed the capabilities of even the most promising single-phase liquid cooling technologies, forcing system designers to seek alternative schemes that rely on two-phase cooling in order to take full advantage of the coolant's both sensible and latent heat (rather than sensible heat alone for single-phase liquid cooling technologies).

In two-phase systems, heat is first extracted from heat-dissipating devices by boiling and rejected to the ambient by condensation. Given the stringent volume and weight limitations in most high-heat-flux applications, both the boiling and condensation must be tackled using highly compact architectures. In regards to condensation, the heat in more conventional configurations is rejected directly to ambient air. However, owing to both compact packaging and intense heat removal considerations, several modern applications rely on use of two cooling loops to remove the heat. Here, the heat is first transferred to a liquid-cooled heat exchanger in the system's primary cooling, and then carried away to a remote heat exchanger via a secondary cooling loop, from which it is ultimately released to ambient fluid (air, cooling water, seawater, *etc.*).

Clearly, overall performance of a high-heat-flux cooling system relies on simultaneous enhancement of both boiling and condensation. While several boiling configurations are possible, including pool [7], channel flow [8], mini/micro-channel [9,10], jet-impingement [11], and spray [12,13], recent studies at the Purdue University Boiling and Two-Phase Flow Laboratory (PU-BTPFL) point to the latter three, and combinations thereof [14,15], as most effective candidates for high-heat-flux applications [3].

* Corresponding author.
E-mail address: mudawar@ecn.purdue.edu (I. Mudawar).

https://doi.org/10.1016/j.ijheatmasstransfer.2019.119158
0017-9310/

Nomenclature

a	coefficient defined in production of ω
Bo	Bond number
c_p	specific heat at constant pressure
Δc	grid size
D_h	hydraulic diameter
E	energy per unit mass
F_σ	surface tension force
f	damping factor
G	mass velocity of FC-72
G_w	mass velocity of water
H	height of flow channel's cross-section
h_{fg}	latent heat of vaporization
I	turbulent intensity
k	turbulence kinetic energy
L	channel length
$\dot{m}$	total mass flow rate for cooling module
N	number of channels in cooling module
n	normal vector coordinate
P	pressure
Q	energy source term
q''_{base}	cooling module's base heat flux
q''_w	channel wall heat flux
Re	Reynolds number
S	strain rate
S_ω	parameter defined in Eq. (20)
T	temperature
T_f	fluid temperature
T_{in}	temperature at channel inlet
T_{sat}	saturation temperature
T_w	channel's bottom wall temperature
t	time
Δt	time step
u	velocity
u'	root-mean-square of turbulent velocity
$\bar{u}$	mean velocity
u_τ	friction velocity
W	width of flow channel's cross-section
W_s	width of copper walls separating channels
x	vapor quality; coordinate along channel width
y	distance perpendicular to bottom wall
y^+	dimensionless distance perpendicular to bottom wall
z	stream-wise coordinate

Greek symbols

α	volume fraction; void fraction
β	parameter in Eq. (20)
β^*	parameter in Eq. (18)
γ	mass transfer intensity factor
θ	contact angle
κ	interfacial curvature
λ	thermal conductivity
μ	dynamic viscosity
ν	kinematic viscosity
ρ	density
σ	surface tension; turbulent Prandtl number
τ	tangential vector coordinate
ω	specific dissipation rate

Subscripts

b	bottom thermocouple plane
c	copper
f	liquid
g	vapor
in	flow channel inlet
i, j	x, y coordinate indicators
s	solid (copper)
sat	saturation
t	top thermocouple plane; turbulent
w	channel bottom wall
$water$	water
ω	specific dissipation rate

Use of mini/micro-channel devices to augment both flow boiling and flow condensation has received considerable attention in recent years. These devices provide several performance benefits, including high heat transfer coefficients, high heat flux to volume ratio, and greatly reduced coolant inventory. The most common of mini/micro-channel devices are those employing multiple, parallel channels sharing inlet and outlet plenums. High performance with these devices is borne mostly out of reduced channel hydraulic diameter. While the advantage of reducing hydraulic diameter is readily apparent with single-phase flow, where heat transfer coefficient is inversely proportional to hydraulic diameter [16], similar advantages are also realized with two-phase flow. And, like flow boiling, use of mini/micro-channel condensation devices has received increased attention since the 1990s [17,18].

It must be emphasized that condensation in mini/micro-channels is fundamentally different from that in macro-channels. For, while gravity can play a dominant role in macro-channels, condensation in mini/micro-channels is influenced far more by surface tension and axial shear. Those differences mean models and correlations derived for macro-channels might not be equally valid for mini/micro-channels. This explains the recent increase in number of experimental studies dedicated entirely to understanding dominant fluid flow and heat transfer mechanisms for mini/micro-channel condensation. The ultimate objective here is to provide a basis for developing a variety of predictive tools, including empirical, theoretical and computational.

1.2. Experimental investigations and empirical correlations for flow condensation in mini/micro-channels

Table 1 provides relevant information concerning recent experimental studies on condensation of pure substances in mini/micro channels. Included are details concerning fluid used, channel configuration and shape, hydraulic diameter, D_h, and length, L, as well as mass velocity of condensing fluid, G (or mass flow rate $\dot{m}$), inlet temperature, T_{in}, inlet pressure, P_{in}, saturation temperature based on inlet pressure, T_{sat}, wall heat flux, $q"_w$, wall temperature, T_w, range of quality, x, and mass velocity of cooling water, G_{water} (or mass flow rate $\dot{m}_{water}$). It should be noted that the present study is focused entirely on condensation in mini/micro-channels.

Table 1 shows prior studies have focused on different aspects of flow condensation, including capture of dominant two-phase flow patterns [19–40] and measurement of heat transfer coefficient [18,22,26,27,29,30,33,35,38,39,41–68] and pressure drop [17,18,22,26,27,31,37,41,42,44–46,48,50,51,54,55,57,59-61,63,64,66–71]. Some of the listed studies also include empirical correlations for flow pattern transitions [3,21,22,34,37,72], heat transfer coefficient [18,26,28,30,33,48,53,54,61,63,65,67], and pressure drop [17,18,31,48,63,69].

It must be acknowledged experimental correlations have historically played a vital role in design of condensation hardware. However, given their severe limitations in terms of fluid used and both geometrical and operating parameters, there is obvious reluc-

Table 1
Studies involving experimental investigation and development of empirical correlations for flow condensation in mini/micro-channels.

Author(s)	Fluid(s)	Test section[a]	D_h (mm)	L (mm)	Operating conditions	Comments
Yang and Webb [17] (1996)	R12	H, MP, R	1.564-2.637	-	G = 400-1400 kg/m^{2}s T_{sat} = 25-50°C q''_w = 4-12 kW/m^2 x = 0.12-0.97	Effects of micro-fins on two-phase pressure drop; pressure drop correlation
Yan and Lin [18] (1999)	R134a	H, SP, C	2.00	84	G = 100-200 kg/m^{2}s T_{sat} = 25-50°C q''_w = 10-20 kW/m^2	Parametric effects on heat transfer and pressure drop; correlations for heat transfer and friction factor
Webb and Ermis [41] (2001)	R134a	H, MP, R	0.44-1.56	-	G = 300-1000 kg/m^{2}s T_{sat} = 65°C q''_w = 8 kW/m^2 x = 0.15-0.9	Effects of hydraulic diameter on heat transfer coefficient and pressure gradient
Wang *et al.* [72] (2002)	HFC-134a	H, MP, R	1.46	610	G = 75-750 kg/m^{2}s T_{sat} = 61.5-66°C x = 0.03-0.94	Pattern-specific heat transfer correlations; combined correlation accounting for effects of flow pattern transition
Koyama *et al.* [42] (2003)	R134a	H, MP, R,	0.80, 1.11	865	G = 100-700 kg/m^{2}s T_{sat} = 60.46°C q''_w = 30 kW/m^2	Heat transfer coefficient; pressure drop
Kim *et al.* [43] (2003)	R22, R410a	H, MP, R,	1.41	455	G = 200-600 kg/m^{2}s T_{sat} = 45°C q''_w = 5-15 kW/m^2 x = 0.1-0.9	Heat transfer coefficient
Shin and Kim [44] (2004)	R134a	H, SP, C	0.691	171	G = 100-600 kg/m^{2}s T_{sat} = 40°C q''_w = 5-20 kW/m^2 x = 0.15-0.85	Local heat transfer coefficient; pressure drop
Huai and Koyama [45] (2004)	CO_2	H, MP, C	1.31	500	G = 123-315 kg/m^{2}s T_{sat} = 21.63-31.33°C P_{in} = 6.48-7.3×10^6 Pa q''_w = 1.10-8.12 kW/m^2 x = 0-1	Local heat transfer coefficient; pressure drop
Cavallini *et al.* [46] (2005)	R134a, R410a	H, MP, R,	0.0828	30	G = 150-750 kg/m^{2}s	Heat transfer coefficient; pressure drop
Shin and Kim [47] (2005)	R134a	H, SP, C/R	0.493-1.067	211	G = 100-600 kg/m^{2}s T_{sat} = 40°C q''_w = 5-20 kW/m^2	Effects of heat flux, mass velocity, quality, hydraulic diameter, and channel geometry on heat transfer coefficient
Wu and Cheng [19] (2005)	water	H, MP, T	0.0828	30	G = 475-193 kg/m^{2}s P_{in} = 4.15-1.25×10^5 Pa T_w = 8°C	Flow patterns (fully droplet, droplet/annular/injection/slug-bubbly, annular/injection/slug-bubbly, fully slug-bubbly)
Louahlia-Gualous and Mecheri [20] (2007)	water	H, SP, C	0.78	690	G = 330-1360 kg/m^{2}s T_{sat} = 96.7-99.1°C P_{in} = 7.36×10^4 Pa T_w = 14°C	Flow patterns (annular, slug bubbly, spherical bubbly, wavy); local condensate film thickness; capillary pressure evolution
Wu *et al.* [21] (2007)	water	H, MP, T	0.053-0.128	60	P_{in} = 4.15-1.25×10^5 Pa T_w = 8°C	Flow patterns (annular, injection, slug/bubbly); local wall temperature; correlation for location of injection flow to determine annular and slug/bubbly zones
Hu *et al.* [22] (2007)	water	H, MP, T	0.073-0.237	280	G = 5-45 kg/m^{2}s q''_w = 6-40 kW/m^2	Flow patterns (droplet, droplet/liquid slug, stratified flow with droplets, injection, slug-bubbly); heat transfer coefficient; pressure drop for slug-bubbly zone; correlations for transitions between flow patterns
Quan *et al.* [23] (2008)	water	H, MP, T	0.09-0.136	600	G = 165-243 kg/m^{2}s T_w = 45-75°C	Flow patterns (mist, annular, injection, plug/slug, bubbly); effects of mass velocity and cooling rate on location of transition from annular to plug/slug flow; occurrence frequency of injection flow
Wu *et al.* [48] (2008)	water	H, MP, T	0.0775-0.128	600	$\dot{m}_{water}$ = 3.46 g/s T_{in} = 22°C P_{in} = 2.8×10^5 Pa	Effects of Reynolds number, condensation number and dimensionless hydraulic diameter on condensation Nusselt number (Nu) and two-phase frictional multiplier; correlations for heat transfer coefficient and pressure drop
Zhang *et al.* [24] (2008)	water	H, SP, R	0.03-0.08	5	G = 140-818 kg/m^{2}s T_{in} = 102.5-131.1°C P_{in} = 1.15-2.88×10^5 Pa	Flow patterns (elongated bubble, elliptical bubble); effect of cooling rate on flow patterns; method for controlling size and generation frequency of micro-bubbles

(*continued on next page*)

Table 1 (*continued*)

Author(s)	Fluid(s)	Test section[a]	D_h (mm)	L (mm)	Operating conditions	Comments
Zhang *et al.* [25] (2008)	water	H, MP, R	0.03-0.08	5	G = 109-228 kg/m^{2}s T_{in} = 105.6-122.6°C P_{in} = 1.23-2.15×10^5 Pa	Flow patterns (elongated bubble followed by detaching or detached miniature bubble, annular flow); method for generating miniature bubbles in micro-channels
Dong and Yang [26] (2008)	R141b	H, MP, R	0.0667-0.117	40	G = 50-500 kg/m^{2}s P_{in} = 1.3-4×10^5 Pa T_w = 4.85°C q''_w = 8.75-45.6 kW/m^2	Flow patterns (annular, slug, bubbly); heat transfer coefficient; pressure drop; flow-pattern-based heat transfer model
Matkovic *et al.* [49] (2009)	R32, R134a	H, SP, C	0.96	230	G = 100-1200 kg/m^{2}s T_{sat} = 40°C P_{in} = 1.01-2.47×10^6 Pa	Local heat transfer coefficient
Park and Hrnjak [50] (2009)	CO_2	H, MP, C	0.89	500	G = 200-800 kg/m^{2}s T_{in} = -15 to -25°C q''_w = 7-30.4 kW/m^2	Effects of operating conditions on heat transfer coefficient and pressure drop
Chen *et al.* [27] (2009)	-	H, MP, TRI	0.10-0.25	56.7	T_{in} = 42.1-58.6°C	Flow patterns (droplet, annular, injection, slug-bubbly); location and frequency of injection flow; wall temperature; total pressure drop; average condensation heat transfer coefficient and average Nusselt number
Wu *et al.* [28] (2010)	-	H, MP, R	0.906	56.7	T_{in} = 42.1-58.6°C	Flow patterns (droplet-annular, injection, slug-bubbly); location and frequency of injection flow; Nusselt number correlation
Del Col *et al.* [51] (2010)	R1234yf, R134a	H, SP, C	0.96	230	G = 200-1000 kg/m^{2}s T_{sat} = 40°C T_w = 22-29°C	Local heat transfer; pressure drop for adiabatic two-phase flow
Oh and Son [52] (2011)	R22, R134a, R410a	H, SP, C	1.70	20	G = 450-1050 kg/m^{2}s T_{sat} = 40°C P_{in} = 1.534-2.424×10^6 Pa T_w = 18.9-32.520°C	Heat transfer coefficient
Del Col *et al.* (2011)	R134a	H, SP, S	1.18	230	G = 200-800 kg/m^{2}s T_{sat} = 40°C P_{in} = 1.017×10^6 Pa T_w = 18.9-32.5°C	Effects of channel shape on heat transfer coefficient
Ma *et al.* [29] (2011)	water	H, MP, T	0.134-0.164	500	G = 90-290 kg/m^{2}s T_{in} = 147.8°C T_w = 20°C $\dot{m}_{water}$ = 0.011 g/s	Flow patterns (annular, droplet, injection, intermittent) and transition characteristics; flow pattern maps; correlations for flow pattern transitions; local heat transfer rate
Park *et al.* [53] (2011)	R134a, R236fa, R1234ze	V, MP, R	1.45	260	G = 50-260 kg/m^{2}s T_{sat} = 25-70°C q''_w = 1-62 kW/m^2	Local heat transfer coefficient; Nusselt number correlation
Bohdal *et al.* [54] (2011)	R134a, R404a	H, MP, C	0.31-3.3	1000	G = 100-1300 kg/m^{2}s T_{sat} = 20-40°C q''_w = 1-62 kW/m^2	Heat transfer coefficient; pressure drop; correlation for local heat transfer coefficient
Kim and Mudawar [30] (2012)	FC-72	H, MP, S	1.0	299	G = 68-186 kg/m^{2}s T_{sat} =57.2-62.3°C P_{in} = 1.040-1.324×10^5 Pa q''_w = 4.3-32.1 kW/m^2 G_{water} = 69-138 kg/m^{2}s x = 0-1.17	Flow patterns (smooth-annular, wavy-annular, transition, slug, bubbly); heat transfer coefficient; correlation for heat transfer coefficient in annular pattern
Zhang *et al.* [55] (2012)	R22, R410a, R407c	H, SP, C	1.088-1.289	200	G = 300-600 kg/m^{2}s T_{sat} = 30-40°C q''_w = 5-40 kW/m^2 x = 0.1-0.9	Effects of mass velocity and quality on heat transfer coefficient and pressure drop
Kim *et al.* [31] (2012)	FC-72	H, MP, S	1.0	299	G = 68-186 kg/m^{2}s T_{sat} = 57.2-62.3°C P_{in} = 1.040-1.324×10^5 Pa q''_w = 4.3-32.1 kW/m^2 G_{water} = 69-138 kg/m^{2}s x = 0-1.17	Flow patterns (smooth-annular, wavy-annular, transition, slug, bubbly); pressure drop; model for total pressure drop
Derby *et al.* [56] (2012)	R134a	H, MP, S/TRI/SC	1.0	100	G = 75-450 kg/m^{2}s T_{sat} = 35-45°C P_{in} = 0.887-1.176×10^6 Pa q''_w = 23.5-46 kW/m^2	Effects of mass velocity, average quality, and saturation pressure on heat transfer coefficient
Heo *et al.* [57] (2013)	CO_2	H, MP, R	1.50	450	G = 400-1000 kg/m^{2}s T_{sat} = -5 to 5°C	Effects of operating conditions on heat transfer coefficient and pressure drop
Goss Jr and Passos [58] (2013)	R134a	H, MP, R	0.77	105	G = 230-445 kg/m^{2}s P_{in} = 7.3-9.7×10^5 Pa q''_w = 17-53 kW/m^2	Effects of temperature, heat flux, mass velocity and quality on heat transfer coefficient

(*continued on next page*)

Table 1 (*continued*)

Author(s)	Fluid(s)	Test section[a]	D_h (mm)	L (mm)	Operating conditions	Comments
Al-Hajri *et al.* [59] (2013)	R134a, R245fa	H, SP, R	0.70	170	G = 50-500 kg/m^{2}s T_{sat} = 30-70°C	Average heat transfer coefficient; overall pressure drop
Liu *et al.* [60] (2013)	R152a	H, SP, R/C	0.952, 1.152	336, 352	G = 200-800 kg/m^{2}s T_{sat} = 40-50°C x = 0.1-0.9	Effects of mass velocity, quality and channel geometry on heat transfer and pressure drop
El Achkar *et al.* [32] (2013)	n-pentane	H, MP, S	0.553	208	G = 3-15 kg/m^{2}s T_{sat} = 28-36.06°C P_{in} = 1.013×10^5 Pa T_w = 23°C	Flow patterns (annular, intermittent, spherical bubbles); time-averaged void fraction profile; time averaged quality profile; time-averaged liquid temperature profile; relationship between void fraction and vapor quality in spherical bubbles zone; bubbles detachment frequency; relationship between bubble detachment frequency and mass velocity
Sakamatapan and Wongwises [69] (2014)	R134a	H, MP, R	1.1-1.2	170	G = 345-685 kg/m^{2}s T_{sat} = 35-45°C q''_w = 18-25 kW/m^2	Pressure drop; correlation for two-phase friction factor
Illan-Gomez *et al.* [61] (2015)	R1234yf, R134a	H, MP, S	1.16	259	G = 350-940 kg/m^{2}s T_{sat} = 30-55°C T_w = 25-50°C	Effects of saturation temperature, mass velocity, quality and fluid properties on pressure gradient and heat transfer coefficient; heat transfer model
Goss Jr *et al.* [70] (2015)	R134a	H, MP, C	0.77	105	G = 230-445 kg/m^{2}s T_{sat} = 28-38°C P_{in} = 7.3-9.7×10^5 Pa q''_w = 17-53 kW/m^2	Effects of temperature, heat flux, and mass velocity on pressure drop
Liu and Li [62] (2015)	R32, R152a, R22	H, SP, C/S	0.952-1.304	336-358	G = 200-800 kg/m^{2}s T_{sat} = 30-50°C T_w = 20, 30°C x = 0.1-0.9	Effects of mass velocity, quality, saturation temperature, inlet temperature, channel diameter, channel geometry, and thermophysical properties on heat transfer coefficient
Kaew-On *et al.* [33] (2016)	R134a	H, SP, C	1.16-3.51	400	G = 350-900 kg/m^{2}s P_{in} = 8-12×10^5 Pa q''_w = 10-50 kW/m^2 x = 0.1-0.9	Flow patterns (transition, semi-annular, annular, annular mist); effects of mass velocity, heat flux, quality and channel shape on heat transfer; heat transfer correlation
Jige *et al.* [63] (2016)	R134a, R32, R1234ze(E), R410A	H, MP, R	0.76-1.06	600	G = 100-500 kg/m^{2}s T_{sat} = 40-60°C q''_w = 3-15 kW/m^2	Effects of mass velocity, quality, saturation temperature, thermophysical properties and hydraulic diameter on heat transfer coefficient and pressure drop; correlation for frictional pressure drop; model and correlation for condensation heat transfer
Liu *et al.* [64] (2016)	propane, R1234ze(E), R22	H, SP, C/S	0.952-1.085	400-420	G = 200-800 kg/m^{2}s T_{sat} = 40-50°C x = 0.1-0.9	Effects of mass velocity, quality, saturation temperature and channel geometry on heat transfer coefficient and pressure drop
El Mghari and Louahlia-Gualous [35] (2016)	-	H, SP, R	0.306	50	G = 75-160 kg/m^{2}s	Flow patterns (mist, annular, slug, injection/bubbly); local and average condensation heat transfer; effects of capillary number, boiling number, contact angle, heat flux, vapor pressure and hydraulic diameter on condensate film thickness
Wang *et al.* [36] (2017)	R134a, R1234ze(E)	H, MP, R	0.301	50	G = 6-50 kg/m^{2}s T_{sat} = 20-25°C	Flow patterns (annular, steady injection quasi-symmetric wave slug/bubbly); flow pattern transition modes (steady injection, wave-coalescence injection, liquid bridging); length and velocity for bubbles and slugs; flow pattern transition locations and frequencies
Liang *et al.* [37] (2017)	FC-72	H, MP, S	1.0	299	G = 31-61 kg/m^{2}s T_{sat} = 57°C P_{in} = 1.01-1.03×10^5 Pa	Flow patterns (liquid slug, elongated bubble); pressure drop; use of interfacial instability theory to describe transition from annular to slug flow; analytical expressions for bubble and slug lengths for most upstream unit cell; model for axial variations of bubble, slug and unit cell lengths
Ding and Jia [38] (2017)	R410a	H, SP, R	0.67	100	G = 109-1042 kg/m^{2}s T_{sat} = 36-41°C q''_w = 38.3-105 kW/m^2 x = 0-1	Flow patterns (annular, wavy-annular, slug, bubbly); heat transfer coefficient
Rahman *et al.* [65] (2018)	R134a	H, MP, R	0.64-0.81	852	G = 50-200 kg/m^{2}s T_{sat} = 30-35°C q''_w = 8 kW/m^2	Effects of vapor quality, mass velocity, channel geometry, and saturation temperature on heat transfer coefficient; condensation heat transfer correlation

(*continued on next page*)

Table 1 (*continued*)

Author(s)	Fluid(s)	Test section[a]	D_h (mm)	L (mm)	Operating conditions	Comments
Kin [66] (2018)	R410a	H, MP, R	0.78-0.95	50	G = 100-400 kg/m^{2}s T_{sat} = 45°C P_{in} = 27×10^5 Pa q''_w = 3 kW/m^2	Heat transfer; pressure drop
Jige *et al.* [34] (2018)	R32	H, MP, R	0.5-1.0	200	G = 30-400 kg/m^{2}s T_{sat} = 15°C	Effects of mass velocity, quality, and channel size on flow patterns (intermittent, transition, annular); method for flow pattern prediction
Guo *et al.* [67] (2018)	R1234ze(E), R290, R161, R41	H, SP, C	2.0	1900	G = 200-400 kg/m^{2}s T_{sat} = 35-45°C q''_w = 8-30 kW/m^2	Effects of thermophysical properties on heat transfer coefficient and pressure drop at different operating conditions; modified correlation for condensation heat transfer in mini-channels
Al-Zaidi *et al.* [39] (2018)	HFE-7100	H, MP, R	0.57	221	G = 48-126 kg/m^{2}s T_{sat} = 60°C P_{in} = 0.97-1.17×10^5 Pa T_w = 20-40°C	Flow patterns (annular, slug, bubbly); effects of mass velocity, local quality, coolant flow rate and inlet coolant temperature on local heat transfer coefficient
Wang and Li [40] (2018)	R134a	H, MP, O	0.3016	50	G = 60-250 kg/m^{2}s T_{sat} = 31°C P_{in} = 8×10^5 Pa x = 0.1-0.9 $\dot{m}_w$ = 30 g/s	Flow patterns (film wavy, corner wavy, slug, bubbly); wavelength and velocity in thin liquid film and channel corners for different mass velocities, qualities, and cooling methods
Wang and Li [71] (2018)	R134a, R1234ze(E)	H, MP, O	0.3016	50	G = 60-250 kg/m^{2}s T_{sat} = 31-45°C T_w = 5-15°C x = 0.1-0.9	Effects of micro-channel array cooling method, mass velocity, inlet quality, cooling water inlet temperature, and saturation temperature on pressure drop
Knipper *et al.* [68] (2019)	R134a	H, MP, R	0.77-0.91	-	G = 200-800 kg/m^{2}s T_{sat} = 40°C	Heat transfer coefficient; pressure drop

[a] H: horizontal, V: vertical, SP: single port, MP: multiport, B: barrel-shaped, C: circular, N: N-shaped, O: oval, R: rectangular, SC: semi-circular, S: square, TRI: triangular, T: trapezoidal, W: W-shaped

tance to rely on correlations as generalized design tools. To overcome this limitation, recent efforts have focused on development of "universal correlations" based on data bases amassed from the literature for many fluids and broad ranges of all relevant parameters [73–75].

1.3. Theoretical investigations of flow condensation in mini/micro-channels

Theoretical models constitute another approach to predicting liquid-vapor behavior in condensing flows. A vast majority of the modeling efforts center on characterizing fluid flow and heat transfer in the annular flow pattern, which arguably is the simplest to model (mainly because of separation of the liquid and vapor phases). Additionally, annular flow both provides the highest heat transfer coefficients and generally prevails over a large fraction of the condensation length compared to all other flow patterns combined. Here, conservation relations are applied separately to the vapor core and liquid film with appropriate boundary conditions employed at the liquid-vapor interface.

Table 2 shows modeling efforts have focused on different aspects of annular condensation, including liquid film distribution in the cross section [76–80], axial liquid film thickness profile [35,38,80–86], meniscus curvature radius [35,82,85,87,88], condensation length [35,83,87,88], quality [76,77,80], void fraction [86], liquid and vapor flow fields [38,81,82,85], local and average heat transfer coefficient [35,38,76–78,80–86,89–94], and pressure drop [77,81]. Aside from annular flow models, a comparatively small number of modeling efforts have addressed determination of two-phase flow patterns and transitions between patterns [40,79].

1.4. Computational simulations of flow condensation in mini/micro-Channels

Computational fluid dynamics (CFD) has become the method of choice for predicting spatial and temporal characteristics of turbulent single-phase fluid flow and heat transfer. This attribute is the direct result of both improved accuracy of available computational models and enhanced computing speed. However, CFD use to model two-phase systems has lagged significantly behind, given the high complexity of flows involving moving interfaces, let alone very long computing time [95]. This is the reason why recent two-phase CFD efforts have focused on improving predictive accuracy as well as accelerating computing time.

Currently, the vast majority of multi-phase CFD models involve one of two approaches: Euler-Lagrange and Euler-Euler. The Euler-Lagrange approach provides high accuracy in tracking liquid-vapor interfaces and ease of applying interfacial boundary conditions. But despite its ability to accurately predict fluid flow within each phase, the need to mesh moving interfaces greatly complicates application of grid topologies, which is why this approach is limited to rather simple two-phase situations.

The Euler-Euler approach is a comparatively simple means to predicting two-phase flows in which the two phases are treated as interpenetrating media and volume fraction as continuous function of space and time. The Euler-Euler approach is implemented using three types of models: Volume of Fluid (VOF) model, Mixture Model, and Eulerian Model, of which VOF is by far the most popular in recent two-phase CFD studies. The VOF method is applied to a fixed Eulerian mesh in which the interface between two phases is captured using a volume function with a value between 0 and 1, where 0 implies the cell is completely occupied by one phase, and 1 by the other. This model employs a single set of momentum and energy equations to the entire domain.

Regardless of the CFD method used, condensing flows are generally very time consuming since condensation processes of practical interest occur in long channels and at relatively high velocity, let alone the temporal fluctuations of the liquid-vapor interface. That is the reason why most CFD condensation studies have been focused on the annular flow pattern. Table 3 provides a summary of recent studies involving CFD modeling of flow condensation in

Table 2
Studies involving theoretical modeling of flow condensation in mini/micro-channels.

Author(s)	Fluid(s)	Geometrical model[b]	Operating conditions	Comments
Liao and Zhao [119] (2002)	Steam	V, SP, TRI (3D) D_h = 0.58-1.16 mm	T_{sat} = 100°C T_w = 94-96°C	Liquid film thickness profile; heat transfer coefficient; pressure drop
Wang *et al.* [76] (2004)	R134a	H, SP, S/TRI (3D) D_h = 1.0 mm L = 600 mm	G = 500 kg/m^{2}s T_{sat} = 50°C T_w = 44°C	Flow patterns (spanwise and streamwise profiles of condensate film), streamwise variation of quality; local and average heat transfer coefficients
Wang and Rose [80] (2005)	R134a, R22, R410a	H, SP, S/TRI/R (3D) D_h = 0.5-5 mm L = 600 mm	G = 100-1300 kg/m^{2}s T_{sat} = 50°C T_w = 44°C	Flow patterns (spanwise and streamwise profiles of condensate film), streamwise variation of quality; local and average heat transfer coefficients
Wang and Rose [77] (2006)	R134a, R22, R410a	H, SP, S/TRI/R (3D) D_h = 0.5-5 mm L = 600 mm	G = 100-1300 kg/m^{2}s T_{sat} = 50°C T_w = 44°C	Flow patterns (spanwise and streamwise profiles of condensate film), streamwise variation of quality; local and average heat transfer coefficients
Nebuloni & Thome [86] (2007)	R134a	H, SP, C/TRI/S (2D) D_h = 0.577-1 mm	T_{sat} = 24°C T_w = 23.5°C	Local and mean heat transfer coefficients, liquid film thickness distribution; void fraction
Chen *et al.* [88] (2008)	-	H, SP, TRI (3D) D_h = 0.1-0.45 mm	P_{in} = 2-3×10^5 Pa q''_w = 50-250 kW/m^2	Condensation length; meniscus curvature radius distribution
Chen *et al.* [87] (2009)	-	H, SP, R/S/TRI (3D) D_h = 0.1 mm	P_{in} = 2×10^5 Pa q''_w = 100 kW/m^2	Condensation length; distributions of curvature radius, pressure and velocity
Agarwal *et al.* (2010)	R134a	H, MP, B/N/R/S/TRI/W D_h = 0.424-0.839 mm L = 406.8 mm	G = 150-750 kg/m^{2}s T_{sat} = 55°C P_{in} = 1.017×10^6 Pa T_w = 18.9-32.5°C	Annular flow heat transfer coefficient model
Bandhauer *et al.* (2006)	R134a	H, MP, C D_h = 0.506-1.524 mm L = 406.8 mm	G = 150-750 kg/m^{2}s T_{sat} = 55°C P_{in} = 1.017×10^6 Pa T_w = 18.9-32.5°C	Heat transfer coefficient
Wu *et al.* [82] (2009)	-	H, SP, R (3D) D_h = 0.1 mm	T_{sat} = 120°C P_{in} = 2×10^5 Pa q''_w = 300 kW/m^2	Distributions of meniscus curvature radius, film thickness, heat transfer coefficient, and wall temperature
Nebuloni and Thome [90] (2010)	R134a, ammonia	H, SP, C/E/FL/F (3D) D_h = 0.01-3.0 mm	T_{sat} = 100°C	Local and perimeter averaged heat transfer coefficients; film thickness distribution; void fraction; mean vapor quality
Wang and Rose [78] (2011)	R134a, R410a, R32, R152a, ammonia, propane	H, SP, S/TRI (3D) D_h = 1 mm	G = 100-1300 kg/m^{2}s T_{sat} = 50°C T_w = 40-48°C	Condensate film distribution; heat transfer coefficient
Kim and Mudawar [81] (2012)	FC-72	H, MP, S (3D) D_h = 1 mm	G = 248-367 kg/m^{2}s T_{sat} = 57.2-62.3°C $\dot{m}_w$ = 3-6 g/s x = 0.23-1.0	Effects of turbulent damping term on eddy momentum diffusivity; velocity and temperature distributions across film; effects of mass flux on liquid film Reynolds number, vapor core Reynolds number, interfacial shear stress, liquid film thickness, local heat transfer coefficient and pressure drop
Hao *et al.* [79] (2013)	R134a	H, SP, R/S/T/TRI (3D) D_h = 0.1-0.333 mm L = 50-56.7 mm	G = 25-300 kg/m^{2}s T_{sat} = 50°C q''_w = 25-60 kW/m^2	Liquid distribution along micro-channels; location for transition from annular to intermittent flow
El Mghari *et al.* [83] (2014)	R134a, R22, R410a	H, SP, S/TRI (2D) D_h = 0.08-0.25 mm L = 1500 mm	G = 80-160 kg/m^{2}s	Effects of hydraulic diameter on average heat transfer coefficient and condensate film thickness; Influence of contact angle and micro-channel shape on Nusselt number and condensation length
Shah [92] (2016)	13 fluids	SP/MP, C/S/R/SC/TRI/B D_h = 0.1-2.8 mm	G = 20-1400 kg/m^{2}s	Correlation for heat transfer coefficient
Shah [91] (2016)	33 fluids	All orientations D_h = 0.1-249 mm	G = 1.1-1400 kg/m^{2}s	Two correlations for heat transfer coefficient
El Mghari and Louahlia-Gualous [35] (2016)		H, SP, R (2D) D_h = 0.305 mm L = 50 mm	G = 75-160 kg/m^{2}s	Flow pattern-based model for condensation heat transfer; distributions of meniscus curvature radius, condensation length and film thickness
Ding and Jia [38] (2017)	R410a	H, SP, R D_h = 0.367 mm L = 100 mm	G = 109-1042 kg/m^{2}s T_{sat} = 36-41°C q''_w = 38.3-105 kW/m^2	Condensate film thickness; dimensionless liquid flow velocity; local and average heat transfer coefficients
Wang and Li [40] (2018)	R134a	D_h = 0.3016 mm L = 50 mm	G = 60-250 kg/m^{2}s T_{sat} = 31°C P_{in} = 8×10^5 Pa $\dot{m}_w$ = 30 g/s x = 0.1-0.9	System instability response to various perturbation wavelengths
Wang *et al.* [84] (2018)	R1234ze(E), R134a	H, SP, O (2D)	G = 300-1500 kg/m^{2}s T_{sat} = 25°C T_w = 10°C	Local heat transfer coefficient; circumferential mean heat transfer coefficient; film thickness
Ding *et al.* [85] (2019)	R410a	H, SP, R (3D) D_h = 0.67 mm	G = 100-1000 kg/m^{2}s T_{sat} = 36°C P_{in} = 2.19×10^6 Pa T_w = 28.5-32.4°C	Liquid film thickness; mass flow rate along sidewall; liquid flow velocity in meniscus region; local and average heat transfer coefficients
Shah [93] (2019)	33 fluids	H/V D_h = 0.10-249 mm	G = 1.1-1400 kg/m^{2}s	Improved correlation for heat transfer coefficient

[b] H: horizontal, V: vertical, SP: single port, MP: multiport, B: barrel-shaped, C: circular, E: elliptical, FL: flower, F: flattened, N: N-shaped, R: rectangular, SC: semi-circular, S: square, TRI: triangular, T: trapezoidal, W: W-shaped

Table 3
Studies involving computational simulation of flow condensation in mini/micro-channels.

Authors	Fluid(s)	Computational domain[c]	Operating conditions	Method	Comments
Da Riva and Del Col [96] (2011)	R134a	H/V, SP, C (3D) D_h = 1 mm L = 375 mm	G = 100-800 kg/m^{2}s T_{sat} = 40°C T_w = 30°C	VOF, CSF, SST k-ω, Lee model	Effects of gravity and surface tension on liquid film thickness and local heat transfer coefficients in horizontal and vertical downflow orientations; zero-gravity flow
Ganapathy *et al.* [103] (2013)	R134a	H, SP (2D) D_h = 0.1 mm L = 30 mm	G = 245-615 kg/m^{2}s T_{sat} = 40°C q''_w = 200-800 kW/m^2	VOF, CSF, Sharp interface model	Flow patterns (annular, transition, intermittent); Nusselt number; pressure drop
Bortolin *et al.* [97] (2013)	R134a	H, SP, C/S (3D) D_h = 1 mm L = 130-390 mm	G = 400-800 kg/m^{2}s T_{sat} = 40°C T_w = 30°C	VOF, CSF, SST k-ω, Lee model	Effects of mass velocity, cross sectional shape, surface tension, and gravity on vapor-liquid interface and heat transfer coefficient
Chen *et al.* [102] (2014)	FC-72	H, SP, R (3D) D_h = 1 mm L = 0.3 m	G = 68-150 kg/m^{2}s T_{sat} = 40°C q''_w = 10-30 kW/m^2	VOF, CSF, Lee model	Effects of mass velocity and heat flux on flow patterns (smooth/wavy annular, transition, slug, bubbly), flow and temperature fields, and bubble volume and velocity
Sun *et al.* [105] (2014)	water	H, SP, C (2D) D_h = 0.5 mm L = 5 mm	u_{in} = 0.2-0.8 m/s T_{sat} = 100°C T_w = 80-97°C	VOF, CSF, Sharp interface model	Effects of inlet velocity and wall temperature on flow patterns (stable/periodic annular, flow/slug flow/bubble flow), condensation length and vapor volume
Zhang *et al.* [99] (2016)	R410a, R134a	H, SP, C/F (3D) D_h = 2.39-3.78 mm L = 400 mm	G = 300-600 kg/m^{2}s T_{sat} = 47°C T_w = 37°C	VOF, CSF, SST k-ω, Lee model	Effects of mass velocity, quality and aspect ratio on liquid-vapor interface, stream traces, film thickness, local heat transfer coefficient and pressure gradient
Gu *et al.* [100] (2018)	R1234ze(E) R134a	H, SP, C (2D) D_h = 0.493-4.57 mm L = 30 mm	G = 400-800 kg/m^{2}s T_{sat} = 40°C T_w = 30°C	VOF, CSF, SST k-ω, Lee model	Effects of mass velocity, vapor quality, and tube diameter on local film thickness, velocity field, heat transfer coefficient, and pressure gradient; new pressure drop correlation
Wu and Li [104] (2018)	R32	H, SP, C (3D) D_h = 0.1 mm L =30 mm	G = 100-200 kg/m^{2}s T_{sat} = 40-50°C T_w = 30-40°C	VOF, CSF, SST k-ω, Lee model	Effects of mass velocity, saturation temperature and wall temperature on flow patterns (annular, injection, slug, bubbly), local heat flux and wall shear stress
Wen *et al.* [98] (2018)	R1234ze(E)	H, SP, C (3D) D_h = 0.493-4.57 mm	G = 400-800 kg/m^{2}s T_{sat} = 40°C T_w = 30°C	VOF, CSF, SST k-ω, Lee model	Effects of mass velocity, quality and diameter on heat transfer coefficient; Relative roles of surface tension, gravity and shear stress in mini/macro-channels and turbulence in liquid phase
Gu *et al.* [101] (2019)	R1234ze(E)	H, SP, C/S/TRI (3D) D_h = 1.21-2 mm L = 150-300 mm	G = 400-800 kg/m^{2}s T_{sat} = 40°C T_w = 30°C	VOF, CSF, SST k-ω, Lee model	Effect of tube shape on liquid-vapor interface, local film thickness and stream traces, axial velocity, heat transfer coefficient, pressure drop
Present study	FC-72	H, SP, S (3D) D_h = 1 mm L = 300 mm	G = 68-367 kg/m^{2}s T_{sat} = 57.2-62.3°C $\dot{m}_w$ = 3-6 g/s x = 0-1	VOF, CSF, SST k-ω, Lee model	Effects of mass velocity, heat flux and saturation temperature on flow patterns (smooth annular, wavy annular, injection, slug, bubbly), wall temperature, quality and local heat transfer coefficient

[c] H: horizontal, V: vertical, SP: single port, C: circular, F: flattened, R: rectangular, S: square, TRI: triangular

mini/micro-channels. Focus topics include relative significance of surface tension and gravity [96–98], turbulence effects [98], effects of operating conditions [96–99], channel's cross-sectional shape [97–101], and channel orientation [96] on liquid and vapor flow fields [100,101], liquid-vapor interface profile [97,99–101], liquid film thickness [96,99–101], heat transfer coefficient [96–101], and pressure drop [99–101].

But, depending on working fluid, geometrical parameters and operating conditions, condensation in channels involves one or multiple flow patterns (pure vapor, smooth-annular, wavy-annular, transition, injection, slug, bubbly, and pure liquid), and both heat transfer and pressure drop characteristics are strongly influenced by these flow patterns. For example, slug flow involves alternating appearance of vapor and liquid phases, complicated by temporal fluctuations in frequency and dimensions of the oblong bubble, as well as appreciable flow field fluctuations in each phase. A few studies have addressed prediction of transient flow patterns [102-105], heat transfer [103,105] and pressure drop characteristics [102] corresponding to flow patterns other than just annular.

1.5. Objectives of study

The primary objective of the present study is to construct a CFD model for condensation in parallel rectangular micro-channels having three-sided cooling walls and corresponding to different values of wall heat flux. Included are detailed formulations of the models and numerical schemes used, along with predictions of time-dependent variations of condensation flow patterns along the flow direction at different operating conditions. In particular, the study details the characteristics of 'injection flow' as a distinctive flow pattern during condensation. The model predictions are validated using experimental results for FC-72, including dominant flow patterns and channel bottom wall temperatures. After the validation, variations of both wall and fluid temperatures both along the flow

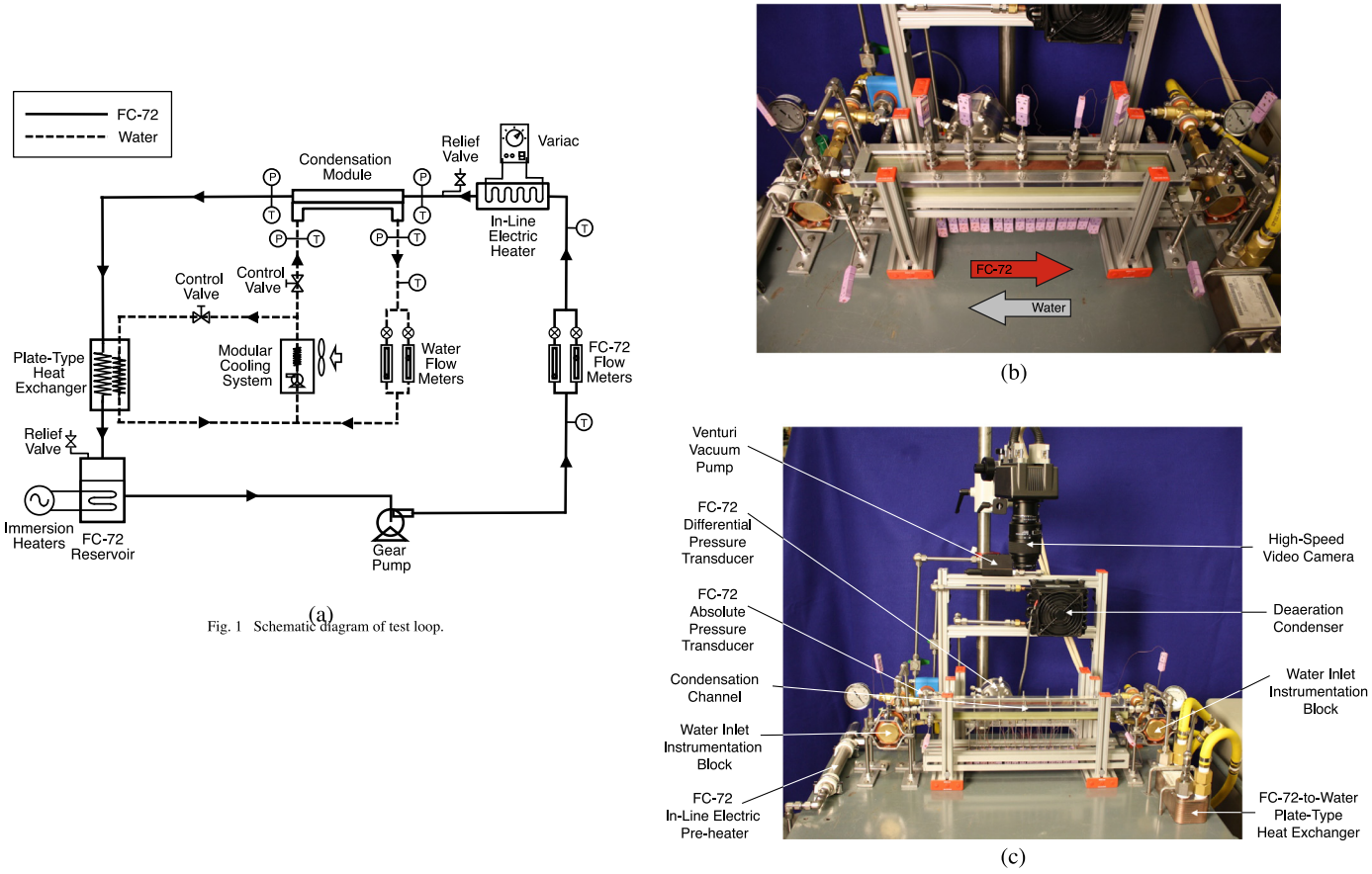

Fig. 1 Schematic diagram of test loop.

Fig. 1. (a) Schematic diagram of the two-phase system, and photos of (a) micro-channel condensation module and (c) main part of test rig.

direction and across the channel width are presented for different operating conditions.

2. Experimental methods

The experimental portion of this study centers on determination of dominant flow patterns and measurement of local bottom channel wall temperatures for flow condensation along parallel micro-channels sharing inlet and outlet plenums. Findings from the experimental study will be compared to predictions of the computational model as basis for model validation. A brief description of the experimental methods used is provided below.

Fig. 1(a)–1(c) illustrate overall construction of the test facility. Shown in Fig. 1(a) is a schematic of the two-phase system, which is comprised of two sub-loops: a primary FC-72 cooling loop and a secondary water loop. In the primary loop, a gear pump is used to supply the FC-72 from a reservoir, passing successively through one of two parallel flow meters and in-line electric heater, before entering the main condensation module. The in-line electric heater serves to bring the FC-72 to slightly superheated state at the inlet to the condensation module. Exiting the condensation module, the FC-72 is condensed further to desired temperature using a water-cooled plate-type heat exchanger.

Cooling water from the secondary loop is supplied through the condensation module in counter-flow direction relative to the FC-72. The water absorbs heat from the condensing FC-72, and is cooled back to desired temperature using a Lytron modular cooling system containing a water pump and a finned-tube water-to-air heat exchanger. Notice in Fig. 1(a) that the Lytron system is also used to cool the FC-72 in the plate-type heat exchanger.

Fig. 1(b) and 1(c) provide photos of the micro-channel condensation module and associated instrumentation. Details of this module are shown schematically in Fig. 2(a) and 2(b), which include a cover plate, insulating housing, condensation copper block, and water channels. Constructed of transparent polycarbonate (Lexan) plastic, the top cover plate both seals the tops of individual micro-channels and provides optical access to the condensing flow. Ten of 1×1 mm^2 square micro-channels are machined into the top surface of the 2 cm wide by 29.9 cm long oxygen-free copper block. The cooling water is supplied through three parallel brass channels soldered to the copper block's underside. Sixteen pairs of type-E thermocouples are embedded at 19-mm intervals along the length of the copper block. The copper block is mounted within a rectangular G-10 plastic housing featuring inlet and outlet plenums, FC-72 inlet and outlet ports, and both pressure and temperature measurement ports. The plenums provide flow area over one order of magnitude larger than the total cross-sectional areas of the parallel micro-channels. Each plenum also features a streamlined ramp to ensure both smooth communication with individual channels and equal distribution of flow rate among the channels.

Experimental data are extracted using parameters indicated in the unit cell depicted in Fig. 2(c), which includes a single micro-channel and half of surrounding copper walls separating micro-channels. Shown are details of the channel: width W and height H (both equal to 1 mm) and copper sidewall width W_s (also equal to 1 mm), which all fall in the range micro-channel flows [10]. The top of the channel is insulated with Lexan plastic, while heat from the channel's side and bottom walls is routed through the copper block beneath and rejected to the cooling water. The micro-channel contains fluid at local axial temperature T_f, and T_w rep-

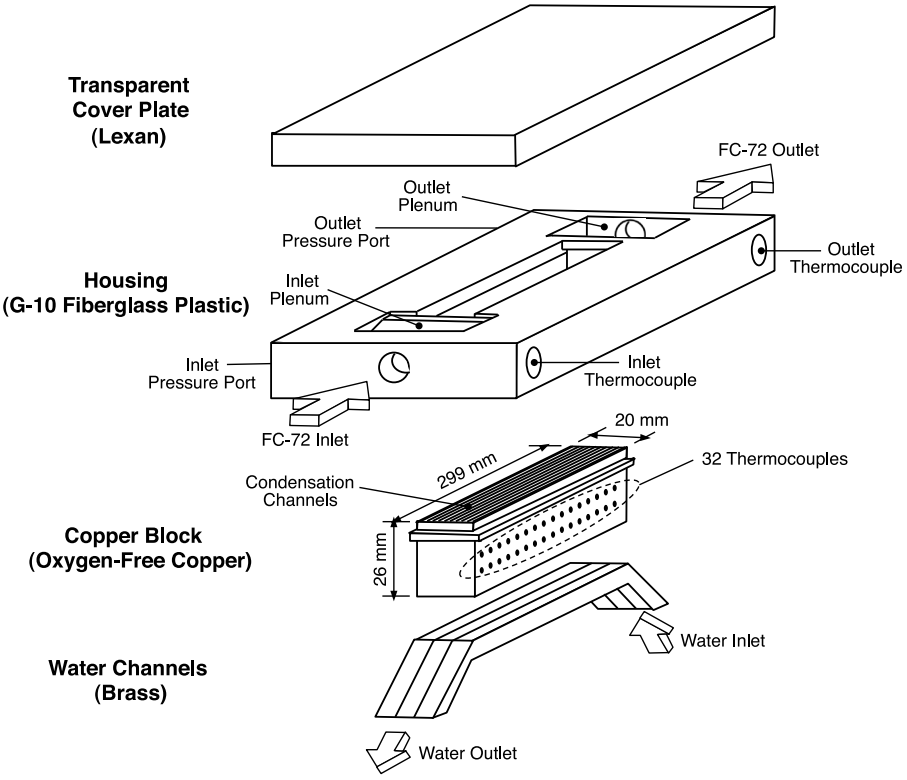

(a)

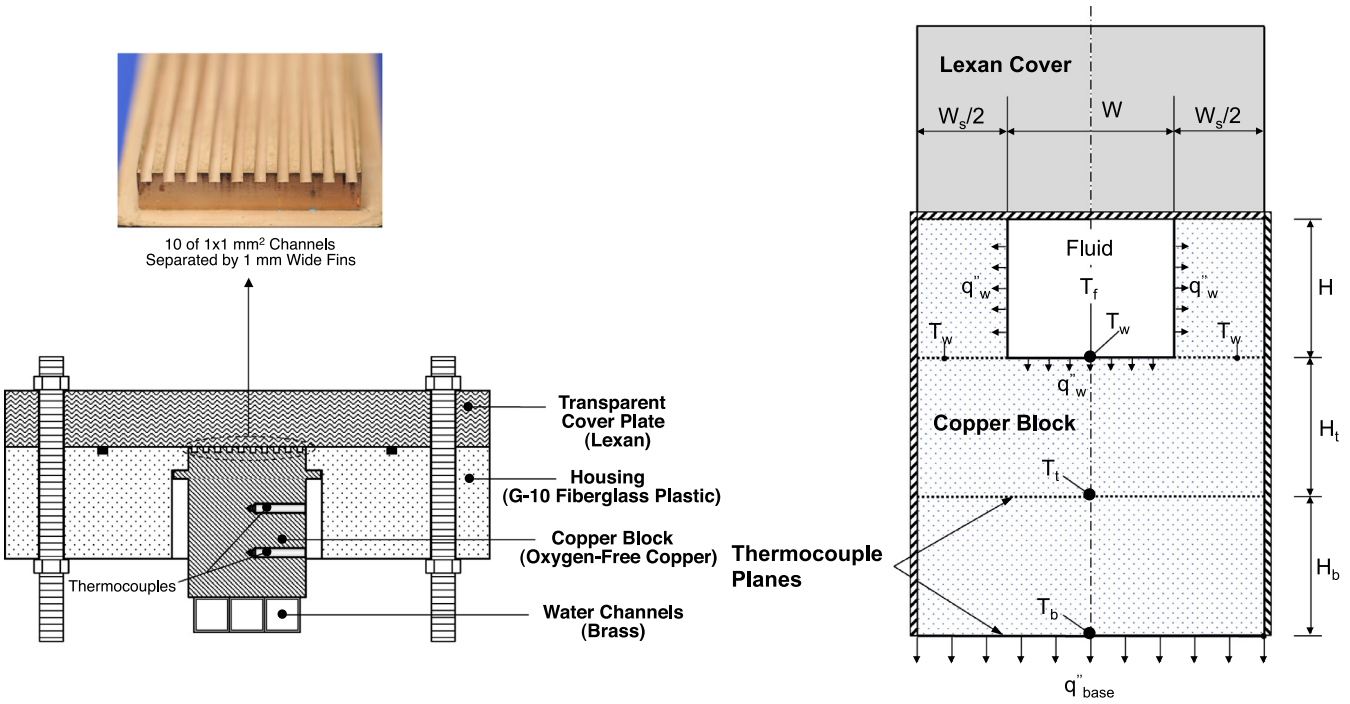

(b) (c)

Fig. 2. (a) Exploded view of micro-channel condensation module. (b) Cross-sectional view of module. (c) Unit cell containing a single micro-channel.

resents the channel's bottom wall temperature. Heat transfer from the channel's three cooling walls is represented by q''_w.

The local heat flux q''_{base} supplied to the bottom of the unit cell is determined using the assumption of one-dimensional heat conduction between the two thermocouple planes,

$$q''_{base} = \frac{\lambda_c (T_t - T_b)}{H_b}, \tag{1}$$

where λ_c, T_t, T_b and H_b are, respectively, thermal conductivity of copper, temperature measured by the top thermocouple, temperature measured by the bottom thermocouple, and vertical distance between the two thermocouples. Use of the assumption of one-dimensional heat conduction is justified by the fact that H_b (= 7.62 mm) and H_t (= 9.65 mm) are much larger than the overall width of the unit cell. The bottom heat flux is used to calculate the channel's bottom wall temperature, T_w, also using the assumption of one-dimensional heat conduction over distance H_t between the planes of T_t and T_w,

$$T_{w,b} = T_t + \frac{q''_{base} H_t}{\lambda_c}. \tag{2}$$

The local rates of sensible heat loss in the short upstream superheated vapor region and latent heat loss in the two-phase condensing region are calculated, respectively, using the energy balances

$$\frac{\dot{m}}{N} c_{p,g}\, \Delta T_f = q''_{base}(W + W_s)\Delta z \tag{3a}$$

and

$$\frac{\dot{m}}{N} h_{fg}\, \Delta x = q''_{base}(W + W_s)\Delta z, \tag{3b}$$

where $\dot{m}$, N, $c_{p,g}$, ΔT_f, Δz, h_{fg}, and Δx are, respectively, total mass flow rate of FC-72, number of parallel channels, specific heat of vapor, incremental axial temperature rise in vapor, differential axial distance, latent heat of vaporization, and incremental axial change in vapor quality. The superheated region maintains single-phase vapor state until the axial location of zero thermodynamic equilibrium quality, therefore

$$x = 1 + \frac{c_{p,g}\left(T_f - T_{sat}\right)}{h_{fg}}, \tag{4}$$

where T_{sat} is saturation temperature based on local saturation pressure. It is important to emphasize that, in all the present experiments, axial span of the upstream superheated region is rather small. This issue will be discussed in more detail in relation to the CFD model development.

Measurement uncertainties of the pressure transducers and flow meters are ±0.5% and ±2.0%, respectively. The thermocouples embedded in the copper block are carefully calibrated to uncertainties below ±0.03°C (see [30,31] for further details). Heat loss through the cover plate is estimated at less than 2% of the heat flow through the micro-channel base plane. For the highest FC-72 mass velocity of G = 367 kg/m^{2}s, derived average uncertainty of base heat is ±4.6%, while, for the worst case corresponding to the lowest mass velocity of G = 68 kg/m^{2}s, the uncertainty increases to ±10.7%.

3. Numerical methods

3.1. Mathematical representation and numerical details

The present study employs the transient Volume of Fluid (VOF) model in ANSYS FLUENT [106] for tracking interfacial behavior during flow condensation, accounting for mass transfer between the two phases. Tracking of interface throughout the computational domain is accomplished by solving continuity equation for volume fraction.

In the present study, major assumptions adopted in the VOF model are as following:

(a) The fluid is incompressible.
(b) Thermal properties of each phase (density, viscosity, thermal conductivity and specific heat) are constant.
(c) Both surface tension and latent heat are constant.
(d) Gravity effects are neglected.
(e) Mass is transferred at the interface between the vapor and liquid phases.
(f) The interface is maintained at saturation temperature of the vapor.

It is important to comment about neglect of gravity effects. This assumption has been verified by many prior micro-channel condensation studies. A key reason for this assumption is that micro-channels greatly increase flow velocity for a given flow rate, rendering gravity effects (which are important for macro-channels) quite insignificant compared to both flow inertia and surface tension. It is for these reasons that many prior investigators opted to neglect gravity effects altogether in their simulations of micro-channel condensation [79,81,87,88,104,105].

The VOF model tracks volume fractions of the liquid and vapor phases in each computational cell and solves conservation equations for both phases. The sum of volume fractions of liquid and vapor in each control volume is equal to unity,

$$\alpha_f + \alpha_g = 1, \tag{5}$$

and $\alpha_f = 1$ and $\alpha_g = 1$ in the interior of the liquid and vapor regions, respectively. Properties in transport equations are shared by both phases in each cell. The density, viscosity and thermal conductivity in each cell are defined, respectively, according to

$$\rho = \alpha_f \rho_f + \left(1 - \alpha_f\right)\rho_g, \tag{6a}$$

$$\mu = \alpha_f \mu_f + \left(1 - \alpha_f\right)\mu_g, \tag{6b}$$

and

$$\lambda = \alpha_f \lambda_f + \left(1 - \alpha_f\right)\lambda_g. \tag{6c}$$

The continuity equations for the liquid and vapor phases are expressed, respectively, as

$$\frac{\partial}{\partial t}\left(\alpha_f \rho_f\right) + \nabla \cdot \left(\alpha_f \rho_f \vec{u}_f\right) = S_f \tag{7a}$$

and

$$\frac{\partial}{\partial t}(\alpha_g \rho_g) + \nabla \cdot (\alpha_g \rho_g \vec{u_g}) = S_g, \tag{7b}$$

where $\vec{u_f}$ and $\vec{u_g}$ are the liquid velocity and vapor velocity, respectively. S_f and S_g are mass source terms (associated with phase change) for the liquid and vapor phases, respectively. The momentum and energy equations are solved for the entire system (including both the liquid and vapor phases) using, respectively,

$$\frac{\partial}{\partial t}(\rho \vec{u}) + \nabla \cdot (\rho \vec{u}\vec{u}) = -\nabla P + \nabla \cdot \left[\mu\left(\nabla \vec{u} + \nabla \vec{u}^T\right)\right] + \vec{F}_\sigma \tag{8}$$

and

$$\frac{\partial}{\partial t}(\rho E) + \nabla \cdot (\vec{u}(\rho E + P)) = \nabla \cdot (\lambda \nabla T) + Q. \tag{9}$$

In the above equations, P, $\vec{F}_\sigma$, E and Q are local pressure, surface tension force, specific internal energy (energy per unit mass), and energy source term (associated with phase change), respectively. The energy source term and specific internal energy are expressed, respectively, as

$$Q = h_{fg} S_f \tag{10}$$

and

$$E = \frac{\alpha_f \rho_f E_f + \alpha_g \rho_g E_g}{\alpha_f \rho_f + \alpha_g \rho_g}. \tag{11}$$

Because of small hydraulic diameter, surface tension force plays an especially important role during condensation in micro-channels. In the present study, this term is calculated using the

Table 4
Operating conditions of present experimental study and computational simulations.

Cases	G (kg/m^{2}s)	G_{water} (kg/m^{2}s)	T_{sat} (°C)	Re_g	Re_f
1	68	138	57.32	5787.23	161.16
2	68	69	57.32	5787.23	161.16
3	118	69	57.78	10031.45	281.40
4	248	69	59.65	20999.15	606.31
5	367	69	61.96	30881.85	924.87

Continuum Surface Force (CSF) model proposed by Brackbill et al. [107],

$$\overrightarrow{F_\sigma} = \sigma \frac{\rho\kappa\nabla\alpha_f}{\frac{1}{2}\left(\rho_f + \rho_g\right)}, \tag{12}$$

where κ is the interfacial curvature, which is calculated according to

$$\kappa = \nabla \cdot \frac{\nabla\alpha_f}{\left|\nabla\alpha_f\right|}. \tag{13}$$

In the VOF model, the liquid-vapor interface normal for a cell near the wall is obtained by specifying contact angle at the wall. The interface normal is given by

$$\hat{n} = \hat{n}_w \cos\theta_w + \hat{\tau}_w \sin\theta_w, \tag{14}$$

where θ_w is the contact angle; a static contact angle value of 10 degrees is used in the present model. $\hat{n}_w$ and $\hat{t}_w$ are unit vectors normal and tangential to the wall, respectively.

As shown in Table 4, which details the operating conditions of the present experimental study, the vapor flow is exclusively turbulent and liquid flow laminar. This fact is reflected by values of all-liquid and all-vapor Reynolds numbers, which are defined, respectively, as

$$Re_f = \frac{G\,D_h}{\mu_f} \tag{15a}$$

and

$$Re_g = \frac{G\,D_h}{\mu_g}, \tag{15b}$$

where G is the mass velocity of FC-72 and D_h the hydraulic diameter. Therefore, an appropriate turbulent model is required to tackle the vapor flow.

Previous investigators adopted a variety of turbulence models in two-phase CFD simulations, which are summarized in Table 3. Many [96–98,100,108,109] demonstrated that the Shear-Stress Transport (SST) k-ω turbulence model [94] (where k and ω are the turbulence kinetic energy and specific dissipation rate, respectively) provides favorable predictions for fluid flow and heat transfer during condensation in micro-channels. The SST k-ω model is a two-equation eddy-viscosity model which is based on the Bradshaw assumption of proportional relationship between turbulent kinetic energy and Reynolds shear stress in the boundary layer [89]. It is crucial to tackle turbulent damping at the interface, which is available only in the k-ω turbulent model. In the SST k-ω model, turbulent viscosity is modified by introducing a limiter to tackle the transport of turbulent shear stress. Following are low-Reynolds number form SST k-ω turbulence model relations adopted in the present simulation,

$$\frac{\partial}{\partial t}(\rho\,k) + \frac{\partial}{\partial x_i}(\rho\,k\,u_i) = \frac{\partial}{\partial x_j}\left(\left(\mu + \frac{\mu_t}{\mathrm{Pr}_{t,k}}\right)\frac{\partial k}{\partial x_j}\right) + \mu_t S^2 - \rho\,\beta^* k\,\omega \tag{16}$$

and

$$\frac{\partial}{\partial t}(\rho\,\omega) + \frac{\partial}{\partial x_j}\left(\rho\omega u_j\right) = \frac{\partial}{\partial x_j}\left(\left(\mu + \frac{\mu_t}{Pr_{t,\omega}}\right)\frac{\partial\omega}{\partial x_j}\right) + \frac{a}{\nu_t}\mu_t S^2 - \rho\beta\omega^2 + 2(1-F_1)\rho\frac{1}{1.168\omega}\frac{\partial k}{\partial x_j}\frac{\partial\omega}{\partial x_j} + S_\omega, \tag{17}$$

where $Pr_{t,k}$ and $Pr_{t,\omega}$ are turbulent Prandtl numbers for k and ω, respectively, μ_t turbulent viscosity, S strain rate, a coefficient associated with production of ω, and ν_t kinematic viscosity. In Eq. (17), β^* and S_ω are defined as follows:

$$\beta^* = 0.09\left(\frac{4/15 + (Re_t/8)^4}{1 + (Re_t/8)^4}\right)[1 + 1.5F(M_t)], \tag{18}$$

where $F(M_t)$ is compressibility function, and turbulent Reynolds number defined as

$$Re_t = \frac{\rho\,k}{\mu\,\omega}, \tag{19}$$

and

$$S_\omega = 2\alpha_i|\nabla\alpha_i|\Delta n\beta\rho_i\left(\frac{f6\mu_i}{\beta\rho_i\Delta n^2}\right)^2. \tag{20}$$

In Eq. (20), α_i is volume fraction of phase i, $|\nabla\alpha_i|$ magnitude of gradient of volume fraction, ∇n cell height normal to interface, f damping factor, and $\beta = 0.075$; μ_i and ρ_i are viscosity and density of phase i, respectively,

3.2. Phase change model

Different phase change models have been used in CFD simulations of condensation processes. The Sharp Interface Model [110], where latent heat is assumed to account for all the heat transferred at the liquid-vapor interface, has been used for simulating interfacial phase change. Ganapathy et al. [103] successfully simulated flow condensation in micro-channels using this model. Sun et al. [105] simplified the Sharp Interface Model by linearizing fluid temperature distribution near the interface and neglecting heat conduction in the vapor core region. Schrage [111] proposed a phase change model where both vapor and liquid cores are in saturated states, but allowed for temperature and pressure jumps across the interface. Tanasawa [112] simplified the Schrage model by assuming interfacial mass flux is linearly dependent on temperature jump between the interface and the vapor phase.

But the phase change model most widely used to determine condensation mass and heat transfer in VOF simulations is the Lee model [113]. The key premise of this model is that phase change is driven by deviation of interfacial temperature from saturation temperature, and phase change rate is proportional to this deviation. Using the Lee model, interfacial mass source terms for the liquid and vapor phases for condensation (different formulation is used for evaporation) is given by

$$S_g = -S_f = \gamma\alpha_g\rho_g\frac{(T - T_{sat})}{T_{sat}} \quad \text{forcondensation}(T < T_{sat}) \tag{21a}$$

$$S_g = -S_f = \gamma\alpha_f\rho_f\frac{(T - T_{sat})}{T_{sat}} \quad \text{forevaporation}(T > T_{sat}), \tag{21b}$$

where γ is called the *mass transfer intensity factor*, the magnitude of which will be addressed later. Eq. (21a) and (21b) indicate, for a given value of γ, that magnitudes of the mass source terms are dependent mainly on void fraction and temperature difference between the cell and interface. For a cell containing vapor ($\alpha_g > 0$), and whose temperature is lower than saturation temperature, the vapor will be transferred to liquid. While, for a cell that is filled with liquid ($\alpha_g = 0$), no mass transfer will occur.

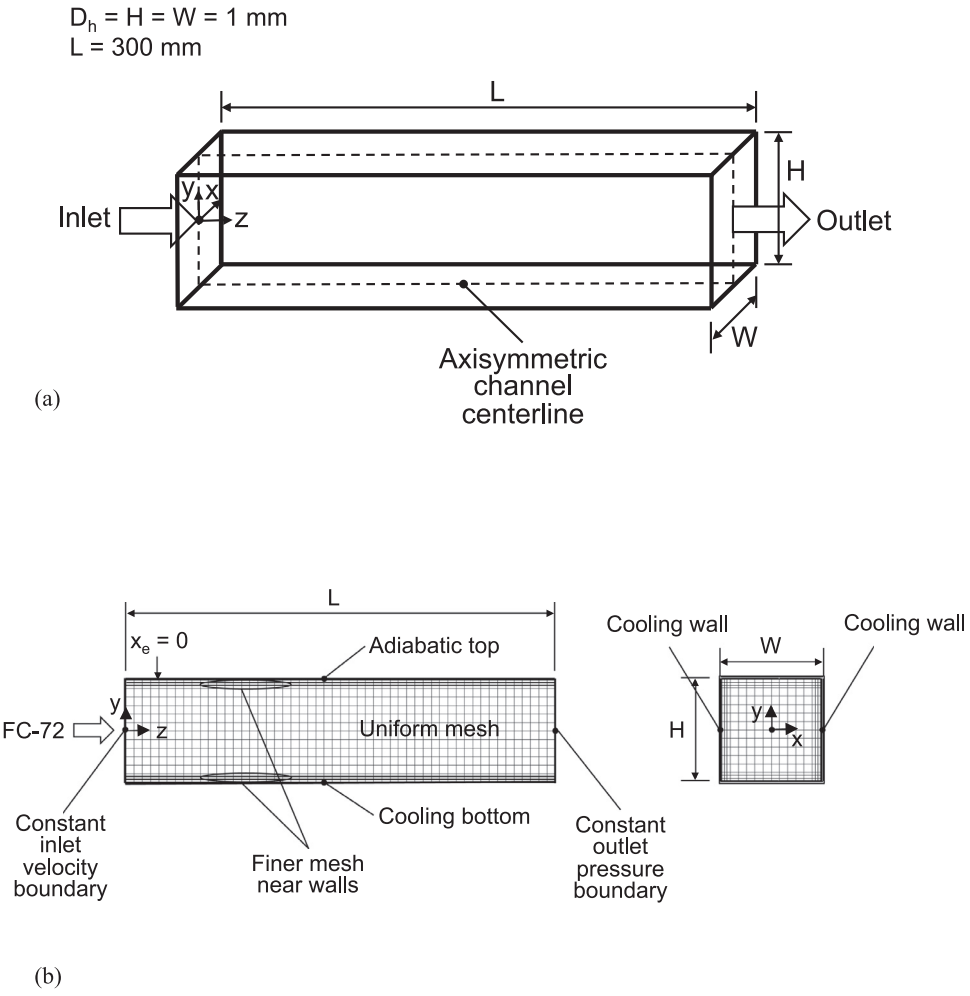

Fig. 3. (a) 3D representation of computational domain. (b) Longitudinal and cross sections of computational domain along with boundary conditions.

Past studies have shown that, when using the Lee model, the value of coefficient γ needs to be carefully adjusted based on system geometry, meshes in computational domain, and operating conditions. Table 5 provides a comprehensive summary of the different values of coefficient γ adopted in prior condensation simulations. Overall, most investigators point out very large γ values tend to produce convergence problems, while very small values result in unrealistically large temperature difference between interface and saturated vapor. This issue will be explored in detail later.

3.3. Computational domain

In present study, a single full channel is used to simulate condensation in parallel micro- channels, with the aim of saving computational time. Fig. 2(c) shows the channel and surrounding material, along with nomenclature for key parameters. Fig. 3(a) shows a 3D representation of the computational domain, which is further detailed in terms of boundary conditions and grid density in Fig. 3(b). The computational domain consists of a horizontal channel having width $W = 1$ mm, height $H = 1$ mm, hydraulic diameter $D_h = 1$ mm, and length $L = 300$ mm, which are actual dimensions of the experimental flow condensation module. To define heat transfer boundary conditions for the channel's cooling walls, the base heat flux q''_{base} is first calculated from the temperature measurements using Eq. (1) as depicted in Fig. 2(c). Piecewise polynomials are then used to fit the variation of q''_{base} with distance z along the channel. This axial variation of q''_{base} is then used to determine local values of the channel's wall heat flux q''_w. The bottom-wall and sidewall cooling boundaries indicated in Fig. 3(b) are assumed to incur constant heat flux equal to q''_w at each axial location. The channel wall and base heat fluxes are related according to

$$q''_w = q''_{base}\frac{W_s + W}{2H + W}. \tag{22}$$

In the same manner, local channel bottom wall temperature T_w is calculated from the temperature measurements using Eq. (2) as shown in Fig. 2(c). Thereafter, piecewise polynomials are used to fit the variation of experimental T_w with distance z along the channel.

The primary measure for accuracy of the present computational model is ability to match predicted axial (z-direction) variation of the channel bottom wall's temperature T_w (averaged along x direction) to the experimentally measured variation. To do so, several combinations of computational adjustments are attempted, most important of which are (1) determining optimum damping factors in the k-ω turbulence model, (2) defining an appropriate value for mass transfer intensity factor γ of the Lee model specific to the present condensation configuration, and (3) ensuring grid independence.

3.4. Damping factor in turbulence model

Fig. 4 shows effects of magnitude of turbulent damping factor f in the k-ω turbulence model on wall temperature predictions for FC-72 and water mass velocities of $G = 248$ kg/m^{2}s and $G_{water} = 69$

Table 5
Summary of different values of coefficient γ of the Lee model used in simulation of condensation in channels.

Authors	Fluid(s)	Geometry	Operating conditions	Mesh	Model	Solutions	γ (s^{-1})
Da Riva and Del Col [96] (2011)	R134a	H/V, C (3D) D_h = 1 mm L = 375 mm	G = 100, 800 kg/m^{2}s T_{sat} = 40°C T_w = 30°C	H FL: 0.8 μm C: 15 μm	Laminar, SST k-ω, CSF	Steady, SIMPLE	7.5×10^5-1×10^7
Liu *et al.* [120] (2012)	Water	(2D) D_h = 4 mm L = 400 mm	u_{in} = 1-3 m/s T_{sat} = 100°C T_w = 25-80°C	Q, 200×50 μm	Laminar, CSF	Transient, Explicit PISO	5000
Bortolin *et al.* [97] (2013)	R134a	H, SP, C/S (3D) D_h = 1 mm L = 130-390 mm	G = 400-800 kg/m^{2}s T_{sat} = 40°C T_w = 30°C	H FL: 0.8-1 μm C: 385-450 nodes	Laminar, SST k-ω, CSF		1×10^6-5×10^6
Chen *et al.* [102] (2014)	FC-72	H, R (3D) D_h = 1 mm L = 300 mm	G = 68-150 kg/m^{2}s T_{sat} = 60°C q''_w = 8.5-30 kW/m^2	H, uniform	Realizable k-ε, CSF	Transient, Explicit PISO	33000
Lee *et al.* [118] (2015)	FC-72	V (2D) D_h = 11.89 mm L = 800 mm	G = 184.4-459 kg/m^{2}s T_{sat} = 63.5-86.6°C P_{in} = 1.086-2.099×10^5 Pa q''_w = 21.1-90.2 kW/m^2	Q FL: 1.3 μm C: 10.3 μm	SST k-ω, CSF	Transient, Explicit PISO	10000
Li *et al.* [108] (2016)	R410a	(3D) D_h = 3.79 mm L = 400 mm	G = 426-1026 kg/m^{2}s T_{sat} = 47°C T_w = 37°C	H	SST k-ω, CSF	Transient	1.5×10^6
Li *et al.* [109] (2017)	R410a	(3D) D_h = 3.79 mm L = 400 mm	G = 426-1026 kg/m^{2}s T_{sat} = 47°C T_w = 37°C	H	SST k-ω, CSF	Transient	1.5×10^6
Zhang *et al.* [99] (2016)	R410a, R134a	H, C/F (3D) D_h = 2.39-3.78 mm L = 400 mm	G = 300-600 kg/m^{2}s T_{sat} = 47°C T_w = 37°C	H	SST k-ω, CSF	Steady	1.5×10^6
Kharangate *et al.* [117] (2016)	FC-72	V (2D) D_h = 11.89 mm L = 800 mm	G = 58.4-271.5 kg/m^{2}s T_{sat} = 69.05-74.55°C P_{in} = 1.045-1.246×10^5 Pa q''_w =21.5-52.3 kW/m^2	Q FL: 2 μm C: 10 μm	SST k-ω, CSF	Transient, Explicit VOF, PISO	10000
Wu and Li [104] (2018)	R32	H, SP, C (3D) D_h = 0.1 mm L = 30 mm	G = 100-200 kg/m^{2}s T_{sat} = 40-50°C T_w = 30-40°C	Q, uniform C: 5 μm	SST k-ω, CSF		3.33×10^9
Gu *et al.* [100] (2018)	R134a, R1234ze(E)	H, C (3D) D_h = 0.493-4.57 mm	G = 400-800 kg/m^{2}s T_{sat} = 40°C T_w = 30°C	H FL: 0.8 μm	SST k-ω, CSF	Steady, SIMPLE	3×10^5 -1.5×10^6
Wen *et al.* [98] (2018)	R134a, R1234ze(E)	H, C (3D) D_h = 0.493-4.57 mm	G = 400-800 kg/m^{2}s T_{sat} = 40°C T_w = 30°C	H FL: 0.8 μm	SST k-ω, CSF	Steady, SIMPLE	3×10^5 -1.5×10^6
Yu *et al.* [121] (2018)	methane, propane	(3D) D_h = 10 mm L = 1400 mm	G = 100-400 kg/m^{2}s P_{in} = 2-4×10^6 Pa q''_w = 3.5-6.5 kW/m^2		RS, CSF	Transient, PISO	1×10^4
Gu *et al.* [101] (2019)	R1234ze(E)	H, C/S/TRI (3D) D_h = 1.21-2 mm L = 150-300 mm	G = 400-800 kg/m^{2}s T_{sat} = 40°C T_w = 30°C	H FL: 0.5 μm	SST k-ω, CSF	Steady, SIMPLE	8×10^5 -3×10^6
Present study	FC-72	H, SP, S (3D) D_h = 1 mm L = 300 mm	G = 68-367 kg/m^{2}s T_w = 57.2-62.3°C $\dot{m}_w$ = 3-6 g/s x = 0-1	H FL: 0.8 μm C: 80 μm	SST k-ω, CSF	Transient, Explicit VOF, PISO	33000

[d]C: core region, FL: first layer, F: flattened, H: hexahedral, Q: quadrilateral

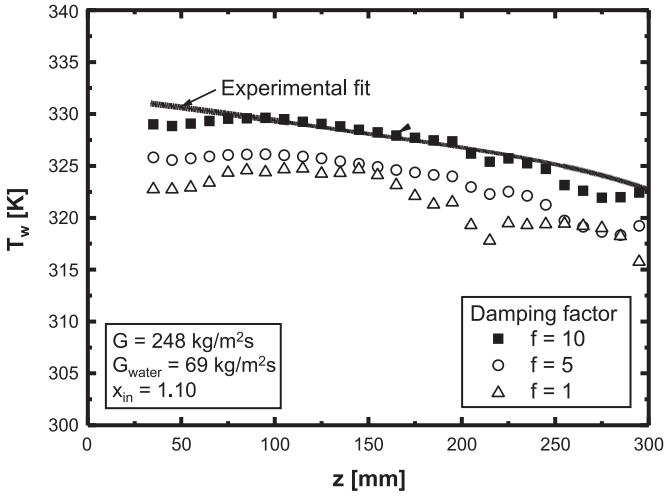

Fig. 4. Determination of optimum damping factor in SST k-ω turbulence model. Wall temperature in this plot is averaged over width W of the channel.

kg/m^{2}s, respectively. Values from 1 to 10 are attempted, and $f = 10$ is shown to provide best predictions. This is also the case for all mass velocities considered, G = 68 to 367 kg/m^{2}s. This value is therefore used throughout the present study.

3.5. Mass transfer intensity factor

As shown in Table 5, prior investigators adopted different values for mass transfer intensity factor γ in the Lee model in pursuit of best predictions of experimental data. To determine optimum value for γ, different values are attempted to achieve best agreement with experimentally determined T_w. Fig. 5(a) shows, for the same operating conditions as Fig. 4, T_w predictions corresponding to different values of γ, while Fig. 5(b) illustrates corresponding interfacial temperature predictions. Clearly, the difference between saturation and interfacial temperatures decreases with increasing value of γ. Notice how lower γ values of 300 and 3000 s^{-1} yield clear deviations from experiment. Far better predictions are achieved as γ is increased to 30,000 s^{-1}. After careful additional adjustment, the value of γ = 33,000 s^{-1} (within a temperature difference of about 1.5K) proved most effective, and this value is therefore maintained throughout the present study.

3.6. Grid independence

Mesh quality can have profound influence on accuracy of computed fluid flow and heat transfer characteristics, and it is therefore essential to ensure independence of predictions from grid size. To do so, different cell sizes are attempted in GAMBIT software [114], and local bottom wall temperatures are numerically predicted and compared with experiment. A non-uniform mesh is built with gradually refined boundary layer mesh near the wall, and further refinement is attempted in ANSYS FLUENT [106].

Fig. 6(a) compares, for G = 367 kg/m^{2}s and G_{water} = 69 kg/m^{2}s, predicted versus measured spatially averaged T_w corresponding to different near-wall cell sizes. Gradual convergence is achieved with decreasing cell size, with $\Delta c = 1$ μm providing excellent convergence. Therefore, cell sizes from 1 and 80 μm are used for wall and core regions throughout the study. This resulted in a computational domain consisting of 867,000 hexahedral cells with corresponding 972,324 nodes.

It is also important to ensure that the first near-wall grid is sufficiently small to accurately capture fluid flow and heat transfer in the wall boundary layer. To do so, mesh refinement near the wall

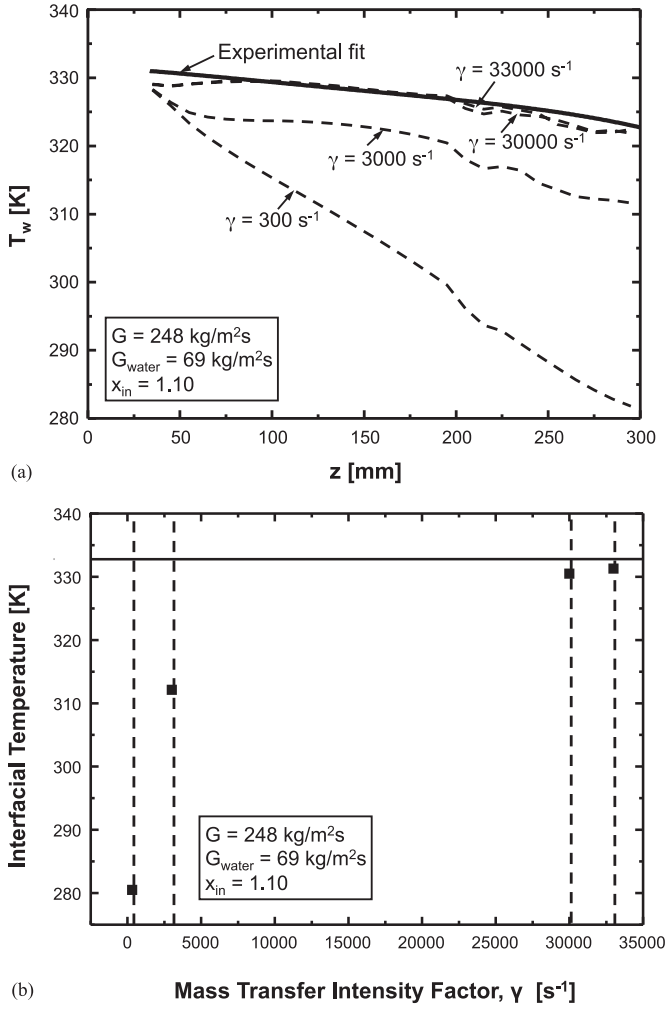

Fig. 5. (a) Determination of optimum mass transfer intensity factor in Lee phase change model (wall temperature in this plot is averaged over width W of the channel). (b) Interfacial temperature predictions corresponding to different values of γ.

is evaluated using non-dimensional distance y^+, which is defined as

$$y^+ = \frac{y u_\tau}{\nu_f}, \tag{23}$$

where y is distance normal to the wall, u_τ friction velocity, and ν_f local kinematic viscosity of the fluid. Fig. 6(b) shows, for same conditions as Fig. 6(a), axial variation of average y^+ corresponding to the near wall Δc of 1 μm. In the present simulations, the average and maximum values of y^+ near the wall are 1.329 and 1.775, respectively, which meet requirements for accurate boundary layer capture.

3.7. Complete model formulation for simulations

All experimental and computational results of the present study concern FC-72. This 3M Company Fluorinert electronic cooling fluid is thermally stable, nonflammable, nontoxic, compatible with most solid materials, and has excellent dielectric properties. It is also very popular as coolant in recent studies on thermal management of electronics, similar to the present. The thermophysical properties of FC-72 are obtained from the NIST Standard Reference Database 23 [115] with representative values listed in Table 6. Thermal properties of the copper wall [116] used in the simulations are provided in Table 7. As indicated earlier, operating conditions for both simulation and experiment are provided in Table 4.

Table 6
Thermophysical properties of FC-72 used in the present simulations.

T_{sat} (°C)	P_{sat} (MPa)	ρ_f (kg/m^3)	ρ_g (kg/m^3)	μ_f (μPa.s)	μ_g (μPa.s)	λ_f (mW/m•K)	λ_g (mW/m•K)	$c_{p,f}$ (kJ/kg•K)	$c_{p,g}$ (kJ/kg•K)	h_{fg} (kJ/kg)	σ (mN/m)
57.32	0.102	1577.8	13.38	421.93	11.750	62.579	13.026	1.098	0.878	84.420	8.1776
57.78	0.103	1576.3	13.59	419.33	11.763	62.535	13.052	1.099	0.878	84.288	8.1326
59.65	0.110	1570.3	14.43	409.03	11.81	62.357	13.160	1.102	0.882	83.750	7.9521
61.96	0.119	1562.8	15.53	396.81	11.884	62.137	13.292	1.106	0.886	83.084	7.7341

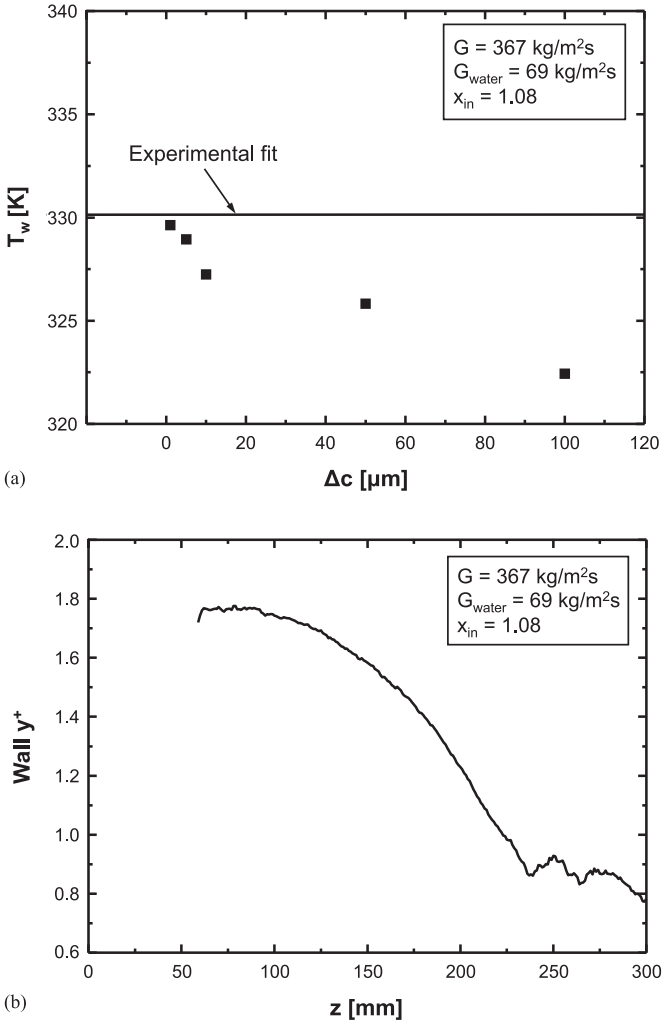

Fig. 6. (a) Grid independent test based on predicted wall temperature (averaged over entire base area of channel). (b) Axial variation of $y+$ (averaged over width W of the channel) for near wall $\otimes c = 1$ μm.

Table 7
Thermal properties of copper used in the present study.

ρ_c (kg/m^3)	$c_{p,c}$ (J/kg•K)	λ_c (W/m•K)
8954	383.1	386

It should be emphasized that in the experiments the fluid enters the condensation module in slightly superheated vapor sate, with thermodynamic equilibrium quality from 1.08 to 1.17. Careful assessment of the short upstream superheated region (4-19% of total channel length, depending on operating conditions) proved exceedingly difficult to model because of difficulty capturing initiation of the annular liquid film in this region. Therefore, all present simulations are on the assumption that the upstream region consists of vapor at saturation temperature from the inlet to the axial location where $x = 1$, at which location the annular film is assumed to begin forming.

In order to reproduce conditions similar to those from the experiments, an adiabatic development length is assumed over the superheated region, which allows the vapor to be maintained at saturation temperature in the same region, while the experimentally determined polynomial curve fit to the wall heat flux is applied from the $x = 1$ location to the end of the channel.

After applying this assumption, simulations were tested corresponding to saturated vapor inlet temperatures of T_{sat} = 57.2 - 62.3°C and FC-72 mass velocities of G = 68 - 367 kg/m^{2}s. A constant velocity profile is assumed at the inlet with turbulent intensity calculated using

$$I = \frac{u'}{\bar{u}} = 0.16\mathrm{Re}_{D_h}^{-1/8}, \tag{24}$$

where u' is root-mean-square of turbulent velocity fluctuation, $\bar{u}$ mean velocity, and Re_{D_h} Reynolds number based on the channel's hydraulic diameter. The temperature and pressure at the outlet are specified from experimental data. The default no-slip condition is applied to all solid walls of the micro-channel. The channel's top wall is treated as adiabatic, and the cooling walls are assumed to maintain constant heat flux q''_w at each axial location, while axial variations of q''_w are determined from polynomial fits to experimental values, as shown in Fig. 7.

The condensation process is simulated using ANSYS FLUENT software, with the VOF model selected and pressure-based approach set as default. A transient solution is sought to capture time dependent variations of flow patterns and heat transfer parameters. Adopted in the time discretization is Explicit Scheme of the VOF model with default factor values for Courant number and volume fraction cutoff, and Geometric Reconstruction Scheme is selected to interpolate face flux. Also employed is the Pressure-Implicit with Splitting of Operators (PISO) pressure-velocity coupling scheme, and the neighbor and skewness corrections are used to improve efficiency. Gradients of variables in the flow conservation equations are computed in accordance with Green-Gauss Cell-Based Gradient Evaluation. The Pressure Staggering Option (PRESTO) is used for interpolating pressure values at the faces. The governing equations are discretized using Implicit Time Integration. Also selected for simulations is Second-Order Upwind Scheme for momentum and energy discretization, First-Order Upwind Scheme for specific dissipation rate and turbulent kinetic energy discretization. A summary of the under-relaxation factors used is provided in Table 8, and convergence criteria for the equation residuals are shown in Table 9.

4. Results and discussion

4.1. Validation of predicted flow characteristics

4.1.1. Flow patterns

Fig. 8 compares condensation flow patterns captured using high-speed video [31] to those predicted by the CFD model. The

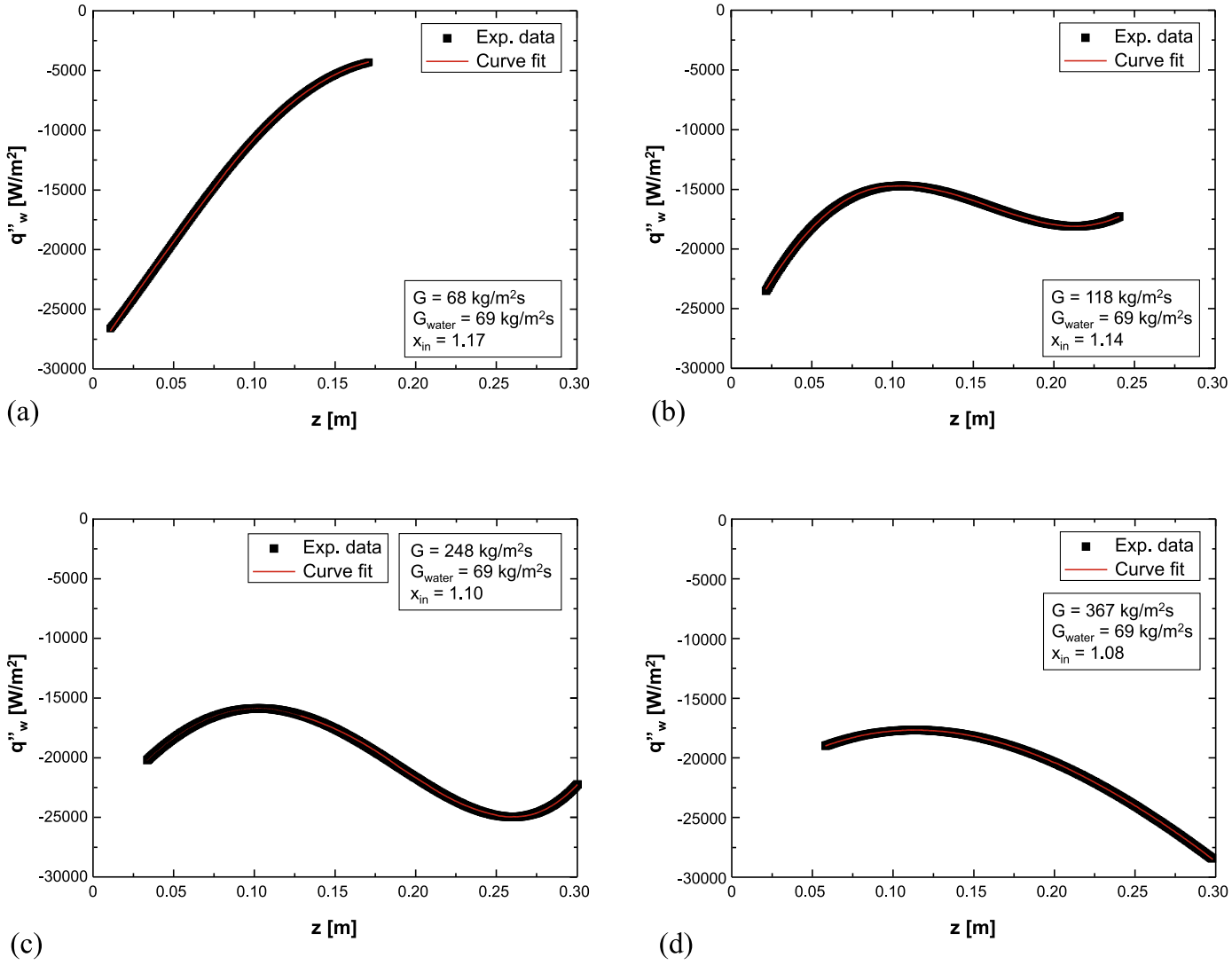

Fig. 7. Experimental and curve fitted axial variations of *q"w* for *Gwater* = 69 kg/m2s and (a) G = 68 kg/m2s, (b) G = 118 kg/m2s, (c) G = 248 kg/m2s, and (d) G = 367 kg/m2s.

Table 8
Under-relaxation factors used in the present study.

Pressure	Density	Body force	Momentum	Turbulent kinetic energy	Turbulent dissipation rate	Turbulent viscosity	Energy
0.3	1	1	0.7	0.8	0.8	1	1

Table 9
Convergence criteria for the equation residuals.

Continuity	*x*-velocity	*y*-velocity	*z*-velocity	Energy	*k*	ω
1×10^{-5}	1×10^{-3}	1×10^{-3}	1×10^{-5}	1×10^{-6}	1×10^{-5}	1×10^{-5}

different patterns correspond to G = 68 kg/m^{2}s, G_{water} = 138 kg/m^{2}s and different axial locations in the y = 0 plane. Four representative flow patterns are shown: *annular, transition, slug* and *bubbly*, which correspond to monotonically decreasing values of vapor quality. The transition pattern corresponds to the downstream end of the annular region where the annular film becomes significantly thicker and wavier, and within which both annular and slug flows occur at the same axial location but different times. Overall, computed interfacial behavior agrees well with experiment for each flow pattern.

Fig. 9(a) provides a more detailed presentation of flow patterns and in-between transitions occurring at different axial location, which are predicted for G = 68 kg/m^{2}s and G_{water} = 138 kg/m^{2}s. Once again, the y = 0 plane is chosen to present the computed flow patterns. Starting with *pure vapor flow* at the inlet, the condensation process is shown commencing upstream with a *smooth-annular* flow pattern, which is characterized by a relatively smooth interface between the cooling wall's condensate film and central vapor core. The condensate film in this region is very thin, which is why it is difficult to distinguish its interface from the solid

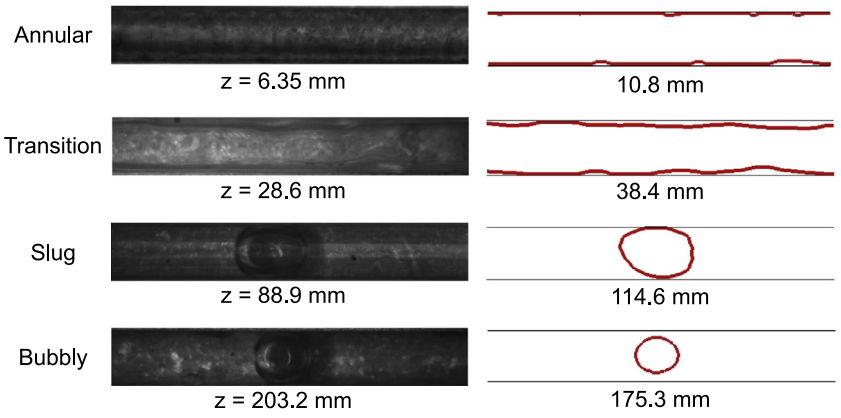

Fig. 8. Comparison of condensation flow patterns captured using high speed video [31] with CFD predictions for G = 68 kg/m2s and *Gwater* = 138 kg/m2s and different axial locations. The CFD predictions correspond to the y = 0 plane along the channel and indicated z-location corresponds to axial center of the video frame.

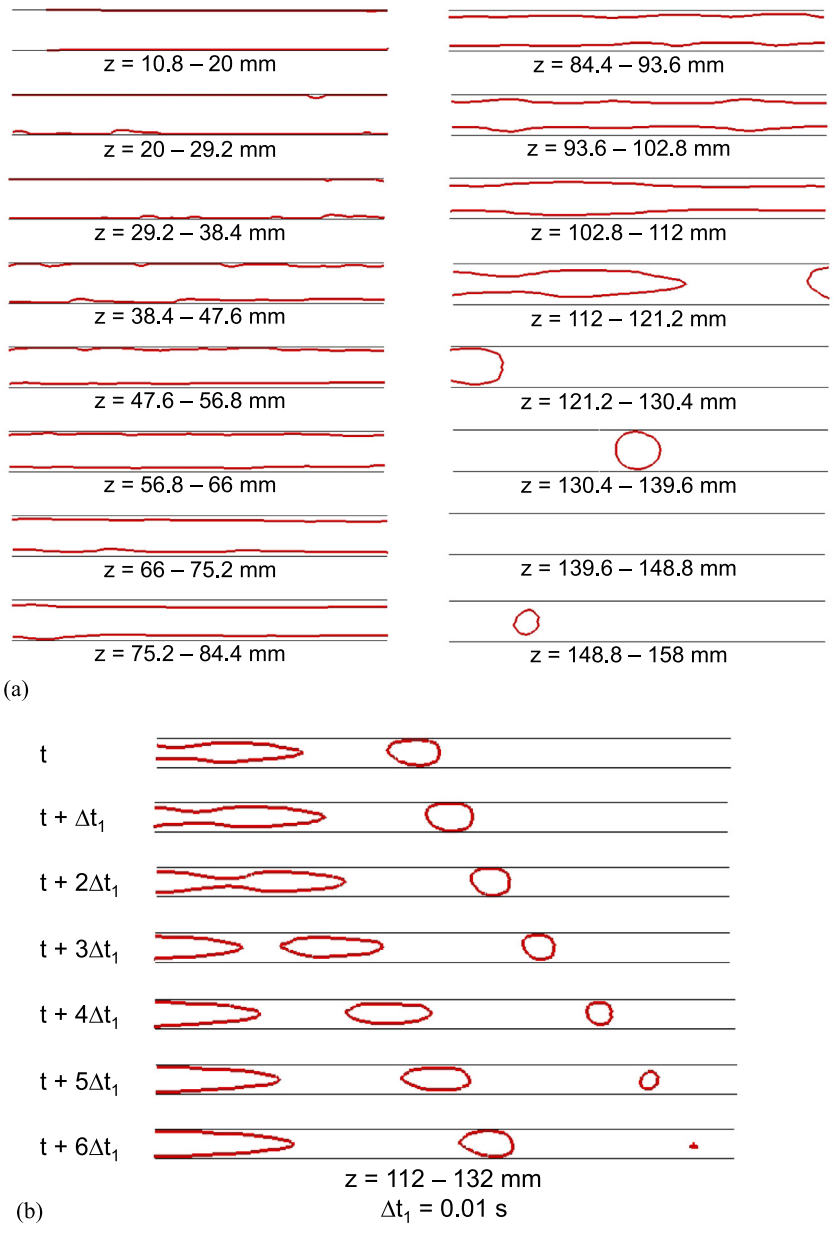

Fig. 9. (a) Predicted flow patterns and (b) process of injection flow for G = 68 kg/m2s and *Gwater* = 138 kg/m2s. The patterns shown correspond to the y = 0 plane.

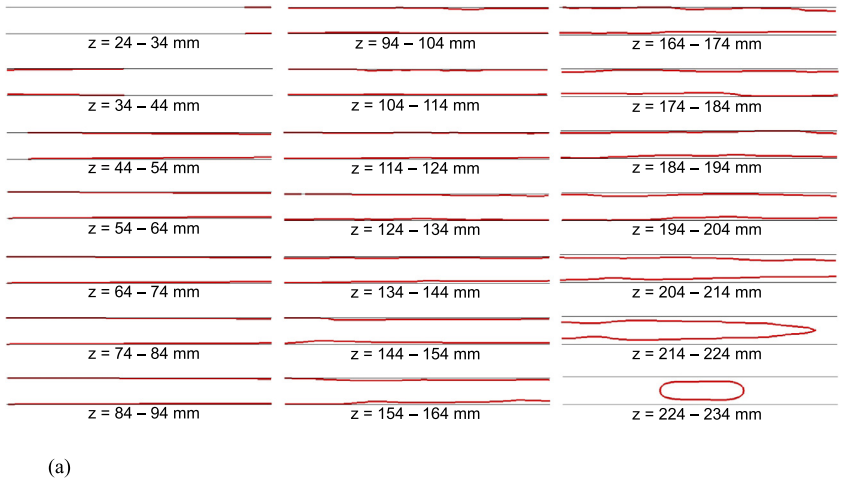

Fig. 10. (a) Predicted flow patterns and (b) process of injection flow for G = 118 kg/m2s and *Gwater* = 69 kg/m2s. The patterns shown correspond to the $y = 0$ plane.

wall. The next flow pattern is *wavy-annular* (~ z = 20-112 mm) which, unlike the smooth-annular pattern, features a thicker annular film whose interface is marred by discernable interfacial waviness. Combined, the *smooth-annular* and *wavy-annular* patterns dominate a significant fraction of the two-phase condensation region. Notice how, with continued cooling/condensation along the channel, the annular liquid film grows even thicker and its interfacial waves more pronounced. *Slug flow* begins to form at ~ z = 112 mm as wave crests of the annular liquid film from opposite walls begin to consolidate, forming discrete liquid slugs separating oblong vapor bubbles whose diameter approaches the channel width and whose length is greater than the channel width. Further axial condensation causes the oblong bubbles to shrink in size until their length approaches the channel width at ~ z = 130.4 mm; this is where the *bubbly flow* pattern is initiated. The bubbles continue to grow smaller along the channel (as shown for z = 139.6 – 158 mm) and eventually condense fully into liquid, signaling onset of *pure liquid flow*.

Fig. 9(b) provides, for same G and G_{water} values as Fig. 9(a), the temporal process of *injection flow*, where, starting with wavy-annular flow, interfacial wave peaks from opposite sides of the channel approach each other, eventually pinching off oblong bubbles downstream and signaling transition from wavy-annular to slug flows.

Fig. 10(a) shows flow patterns predicted in the $y = 0$ plane at different axial positions for a higher FC-72 mass velocity of G = 118 kg/m^{2}s, and lower water mass velocity of G_{water} = 69 kg/m^{2}s. In this case, it takes larger axial span for the vapor to condense, which is evidenced in Fig. 10(a) by the combined smooth-annular and wavy-annular flow patterns extending farther downstream the channel to ~ z = 214 mm (compared to ~ z = 112 mm for G = 68 kg/m^{2}s, Fig. 9(a)). Also evident in Fig. 10(a) is how the injection flow commences farther downstream compared to the lower G case. This is also why slug flow is encountered farther downstream.

Fig. 10(b) shows, for the same FC-72 and water mass velocities as Fig. 10(a), the temporal process of injection flow, which is mechanistically similar to that of the lower G case, except that it occurs much farther downstream.

4.1.2. Flow pattern map

Flow pattern maps are quite popular in two-phase literature because of their ease of use by designers. These maps capture both dominant flow patterns and transition boundaries between patterns for different operating conditions, using a variety of coordinates to demarcate the different patterns. In the present study, a flow pattern map developed in ref. [31], based entirely on high speed video imaging of the condensing flow, is used for validation purposes. Fig. 11 shows this map plotted in an FC-72 mass

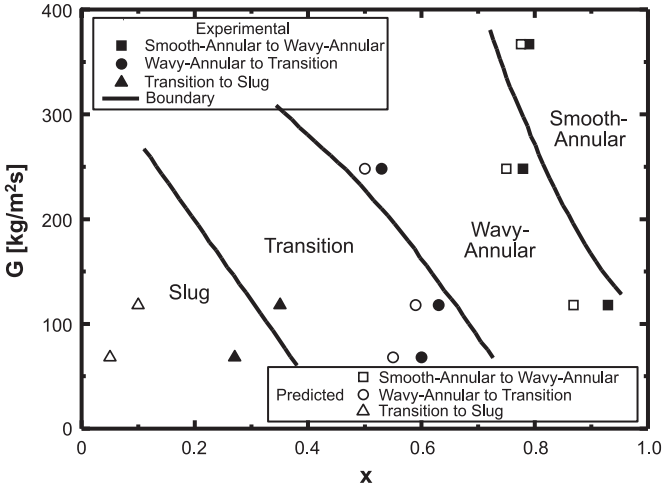

Fig. 11. Comparison of predicted flow pattern transitions with experiment [31].

velocity-quality plane. Superimposed on the original map are both computational predictions (open symbols) from the present study and experimental flow pattern data (solid symbols) for the same operating conditions. It should be noted that the experimental boundary lines are based on a much broader database, much of which is purposely excluded from Fig. 11 to focus only on the operating conditions addressed in the present study. Most obvious in this map is that occurrence of smooth-laminar, wavy-laminar, transition, and slug flow patterns appears to follow a monotonic trend with simultaneous decreases in G and x. Overall, taking into consideration both measurement uncertainties of video capture (as different flow patterns sometimes occur at the same axial location but different times) and assumptions adopted in the present computational method, Fig. 11 shows reasonable agreement with experiment, with most of the departure corresponding to the low G and low x corner of the map.

4.2. Validation of Heat Transfer Characteristics

Accurate prediction of experimental wall temperatures is the primary measure used in the present study for assessment of predictive accuracy of the computational method used. Fig. 12(a)–12(d) compare axial variations of experimental and computed wall temperatures for FC-72 mass velocities of G = 68, 118, 248 and 367 kg/m^{2}s, respectively, all corresponding to the same water mass velocity of G_{water} = 69 kg/m^{2}s. Here, the computed values are averaged over the channel width as well as time after reaching steady state. For all four cases, both experimental and computed values show T_w decreasing monotonically along the channel because of the water cooling. For the case of G = 68 kg/m^{2}s, Fig. 12(a) shows both the data and predictions limited to a relatively smaller fraction of the condensation length, which can be explained by complete condensation to liquid occurring farther upstream than for higher G values. On the other hand, for the cases of G = 248 and 367 kg/m^{2}s, Fig. 12(c) and 12(d), respectively, both data and computed results persist to the end of the channel. An observable difference between experiment and predictions is manifest in Fig. 12(a) for the lowest G value, with a smoother declining trend with z for the former, compared to more fluctuating trend for the latter. This aspect of computed values can be attributed to temporal fluctuations in the form of several flow patterns compressed into a rather smaller axial span of the condensation length. Notice how the fluctuations diminish significantly with increasing G, as individual flow patterns begin to dominate over larger portions of the condensation length. Average deviations of axial wall temperature between computational results and experimental data range from 6.81% to 1.46%, corresponding to FC-72 mass velocities between 68 and 367 kg/m^{2}s. For larger mass velocities, annular flow occupies a large fraction of the channel length, leading to smoother wall temperature predictions. For smaller mass velocities, annular flow appears mostly in the upstream portion of the channel, with transitions between different flow patterns prevailing from about 120 mm, Fig. 9(a), which leads to more discrete changes in wall temperature coupled with relatively higher deviation between computational predictions and experiment. Overall, Fig. 12 shows the present computational method provides good agreement with experimental data in both trend and magnitude. This is further evidence of the effectiveness of computational methods at predicting condensing flows as discussed in other recent references (*e.g.*, [117,118]).

4.3. Further predictions of heat transfer characteristics

One of the primary advantages of computational methods is ability to predict certain parameters and details commonly either impossible or very difficult to obtain experimentally. Shown below are such predictions, which include spatial variations of both wall and fluid temperatures.

4.3.1. Spatial distributions of wall temperature

Fig. 13(a)–13(d) show predicted contour plots of the channel's bottom wall temperature for G = 68, 118, 248 and 367 kg/m^{2}s, respectively. These plots span the entire x-z plane at y = -0.5 mm of the computational domain. As discussed earlier, since the F-72 enters the channel in superheated vapor state, a short upstream region of the channel is subjected to zero heat flux up the location of x = 1 from experiments, and vapor within the upstream region is assumed to maintain saturation temperature. The experimentally determined wall heat flux is applied between the axial location of x = 1 and the outlet. Fig. 13(a) – 13(d) all show the temperature contours are fairly symmetrical around the x = 0 centerline, excepting slight variations resulting from time dependent variations in the predicted values. The wall temperatures decrease monotonically along the channel for all cases due to the cooling effect. The lowest mass velocity (G = 68 kg/m^{2}s) shows comparatively large z-direction gradients, because of faster succession of flow patterns occurring over a smaller upstream portion of the channel length. The apparent downstream increase in wall temperature in Fig. 13(a) must be carefully explained. Recall that the wall heat flux boundary condition used in the computational method is obtained from the experiments. For low G, the wall heat flux decreases sharply in the outlet region as the condensation process ceases and all the fluid is converted into liquid well upstream of the outlet. On the other hand, for the higher mass velocities (G = 248 and 367 kg/m^{2}s), the wall heat flux increases in the outlet region as the condensation process persists all the way to the outlet. This effect is captured Fig. 13(c) and 13(d) in the form of wall temperature decreasing to the outlet. Overall, z-direction variations of both the experimental wall heat flux and computed wall temperatures point to a close relationship between temperature trends and transitions between flow patterns along the channel.

4.3.2. Spatial distributions of fluid temperature

Ability to predict spatial variations of fluid temperature represents another important advantage of using computational methods when modeling flow condensation in channels. Fig. 14(a)–14(d) show, for G = 68, 118, 248 and 367 kg/m^{2}s, respectively, side-by-side plots of fluid temperature (T_f) variations across the channel width and normal to the wall at different axial locations along the channel. The horizontal solid line in each figure represents the

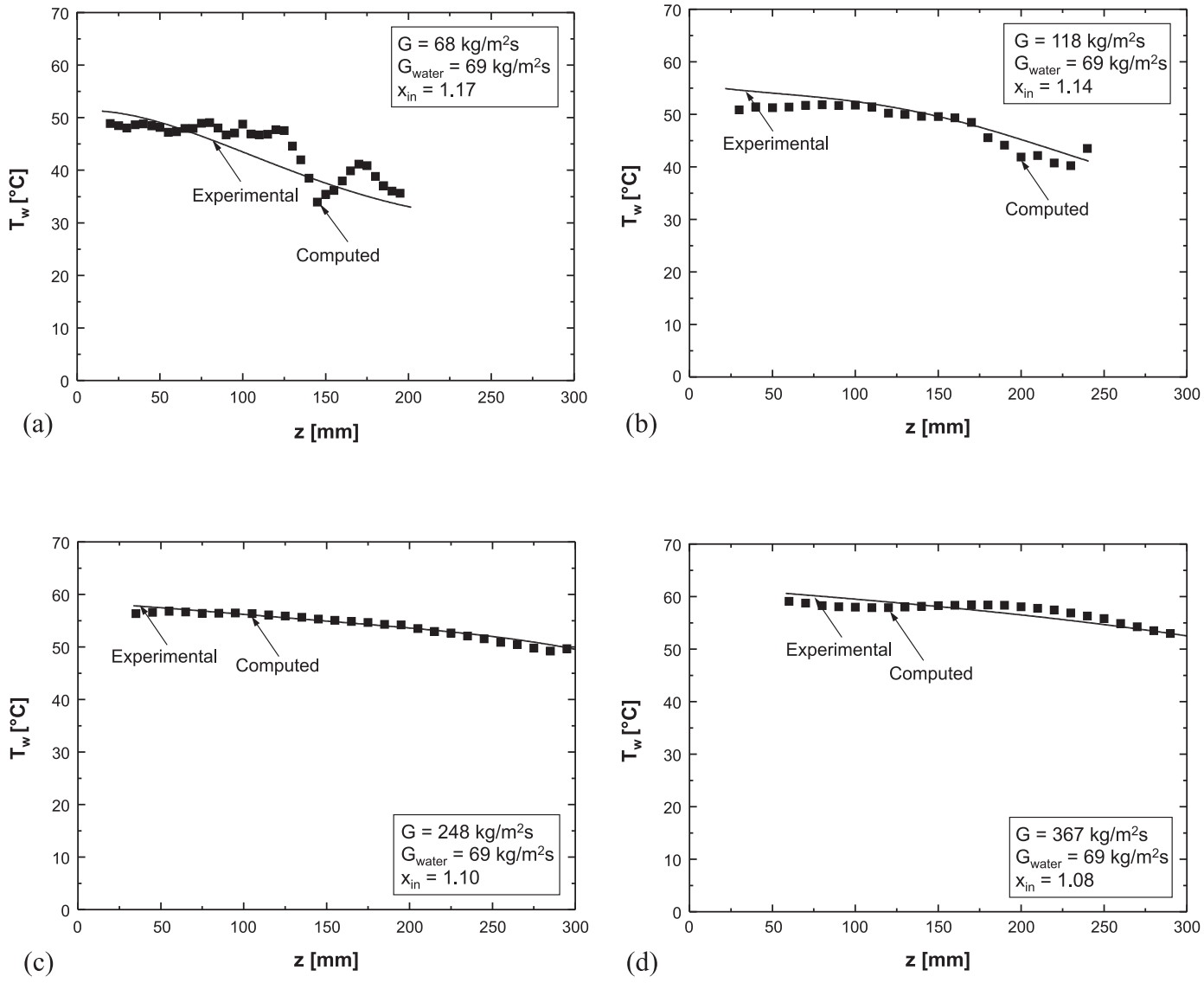

Fig. 12. Comparison of computed axial variation of wall temperature (averaged over channel width W and time) with experiment for *Gwater* = 69 kg/m2s and (a) G = 68 kg/m2s, (b) G = 118 kg/m2s, (c) G = 248 kg/m2s, and (d) G = 367 kg/m2s.

fluid's saturation temperature. For G = 68 kg/m^{2}s, Fig. 14(a) shows comparatively appreciable changes in T_f along the 150-mm upstream portion of the channel length, with fairly noticeable boundary layers along the cooled sidewalls. No further temperature predictions are provided for the downstream region as the entire flow has already been converted to liquid around z = 150 mm. For G = 118 kg/m^{2}s, Fig. 14(b) shows similar trends but relatively smaller axial temperature gradient. Here, predictions are available for z = 250 mm as well because of larger extent of the condensation region. For G = 248 kg/m^{2}s and G = 367 kg/m^{2}s, Fig. 14(c) and 14(d), respectively, T_f predictions are also available for z = 100, 150 and 250 mm. For these high G conditions, axial temperature variations are much smaller than for G = 68 kg/m^{2}s, so are the thicknesses of thermal boundary layers along the sidewalls.

Fig. 15(a)–15(d) show for G = 68, 118, 248 and 367 kg/m^{2}s, respectively, variations of T_f in the x-z plane and y = 0 (halfway along the height of the channel). In each case, as discussed earlier, fluid in the upstream inlet region is shown maintaining saturation temperature before the condensation process commences. The contour plots show fairly symmetrical temperature around the x = 0 centerline, marred only by small differences resulting from time dependent variations in the predicted values. And all four cases show T_f is lower along the cooled sidewalls and decreases monotonically along the condensation length. The rather uniform contours for G = 248 and 367 kg/m^{2}s (Fig. 15(c) and 15(d), respectively) reflect prevalence of the smooth-annular and wavy-annular flow patterns over much of the condensation length.

Fig. 16(a)–16(d) show T_f contour plots for G = 68, 118, 248 and 367 kg/m^{2}s, respectively, in the y-z plane and x = 0 (channel's center plane). For G = 68 kg/m^{2}s, Fig. 16(a) shows T_f gradients concentrated along the channel's bottom wall (y = -0.5 mm), with no gradient along the top insulated wall. Also obvious in the same contour plot is a fairly uniform gradient pattern extending until ~ z = 130 mm; this is the region dominated mostly by smooth-annular and wavy-annular flow patterns. Notice how, downstream from this location, the gradients perpendicular to the bottom wall penetrate deeper away from the wall, as slug and bubbly flow patterns emerge. Then ~ z = 220 mm, gradient penetration subsides appreciably as virtually complete conversion into liquid takes effect. Fig. 16(b) shows similar trends for G = 118 kg/m^{2}s, albeit

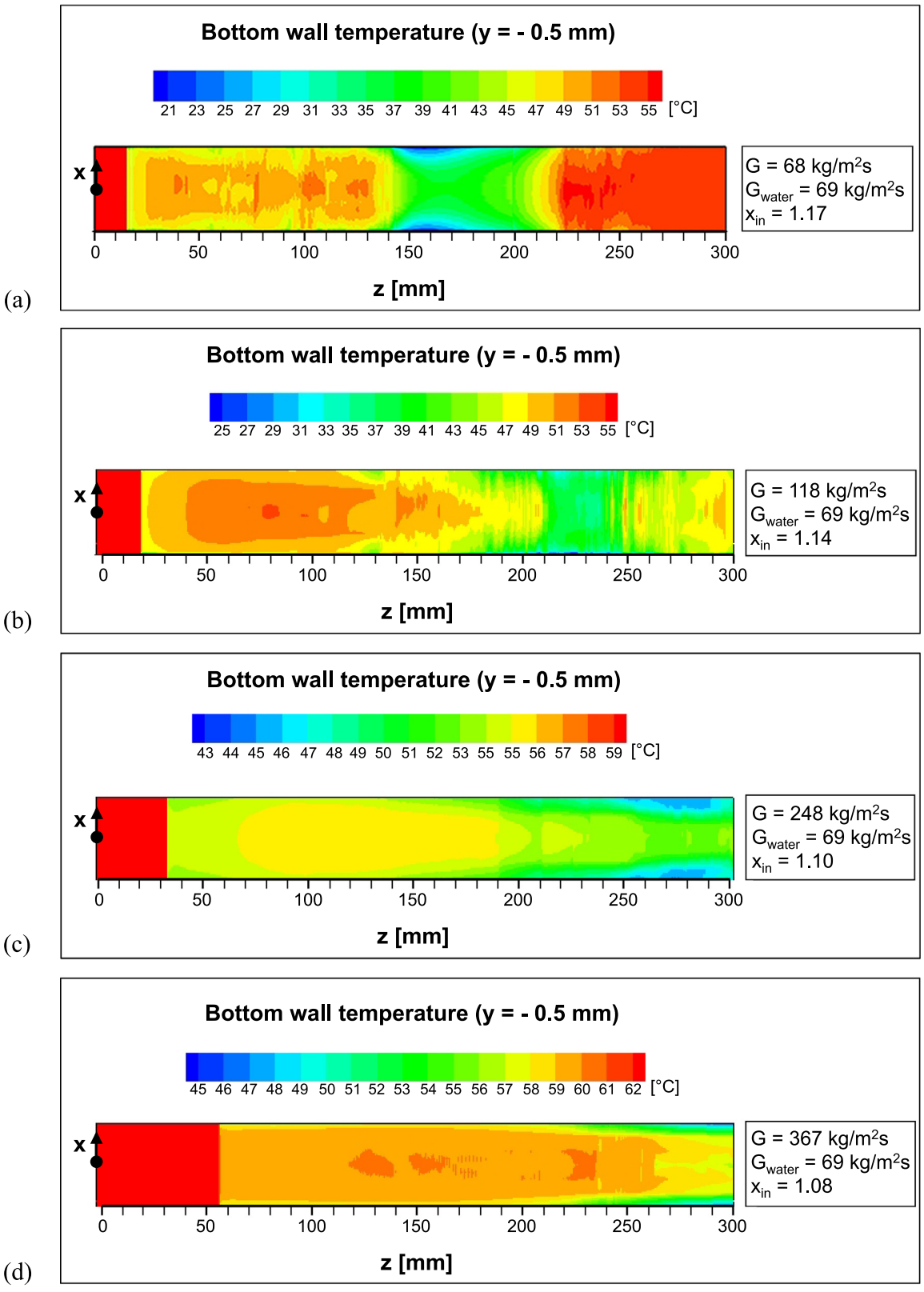

Fig. 13. Contour plots of channel's bottom wall temperature (y = -0.5 mm) for *Gwater* = 69 kg/m2s and (a) G = 68 kg/m2s, (b) G = 118 kg/m2s, (c) G = 248 kg/m2s, and (d) G = 367 kg/m2s.

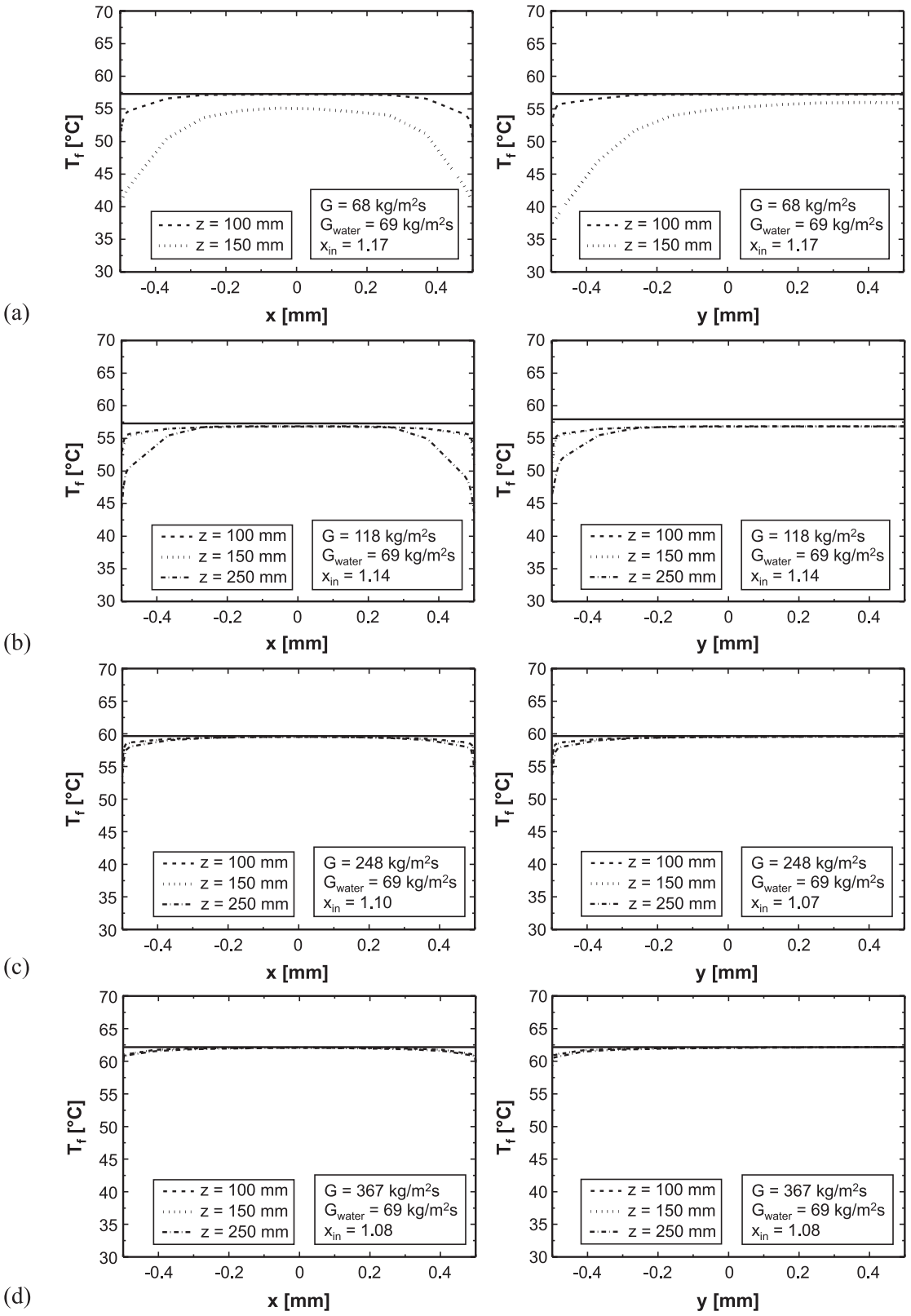

Fig. 14. Variations of computed fluid temperature across width of channel (*Tf* versus *x*, $y = 0$ plane) and height (*Tf* versus *y*, $x = 0$ plane) at different axial *z* locations for *Gwater* = 69 kg/m2s and (a) $G = 68$ kg/m2s, (b) $G = 118$ kg/m2s, (c) $G = 248$ kg/m2s, and (d) $G = 367$ kg/m2s.

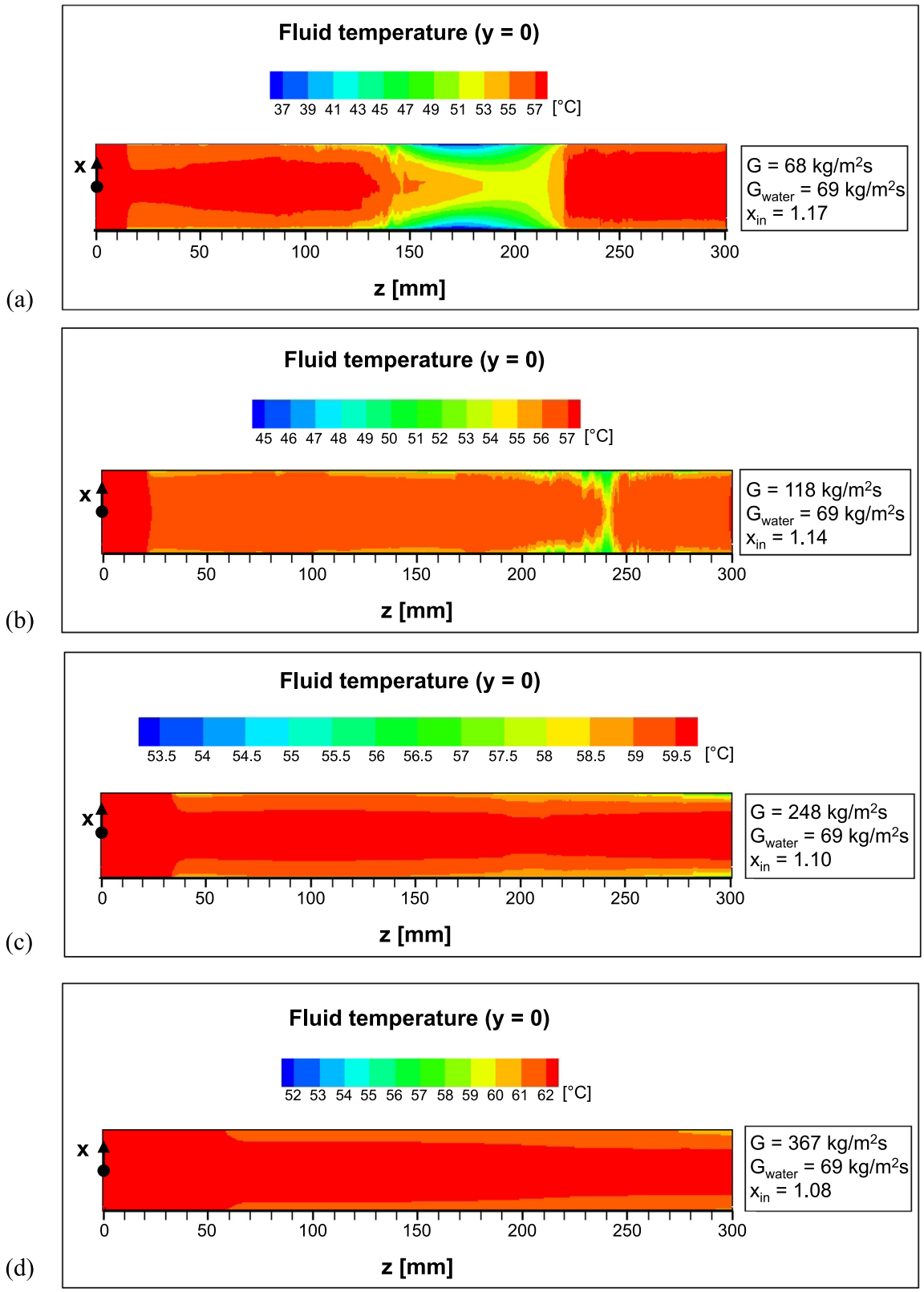

Fig. 15. Contour plots of fluid temperature at $y = 0$ for *Gwater* = 69 kg/m2s and (a) $G = 68$ kg/m2s, (b) $G = 118$ kg/m2s, (c) $G = 248$ kg/m2s, and (d) $G = 367$ kg/m2s.

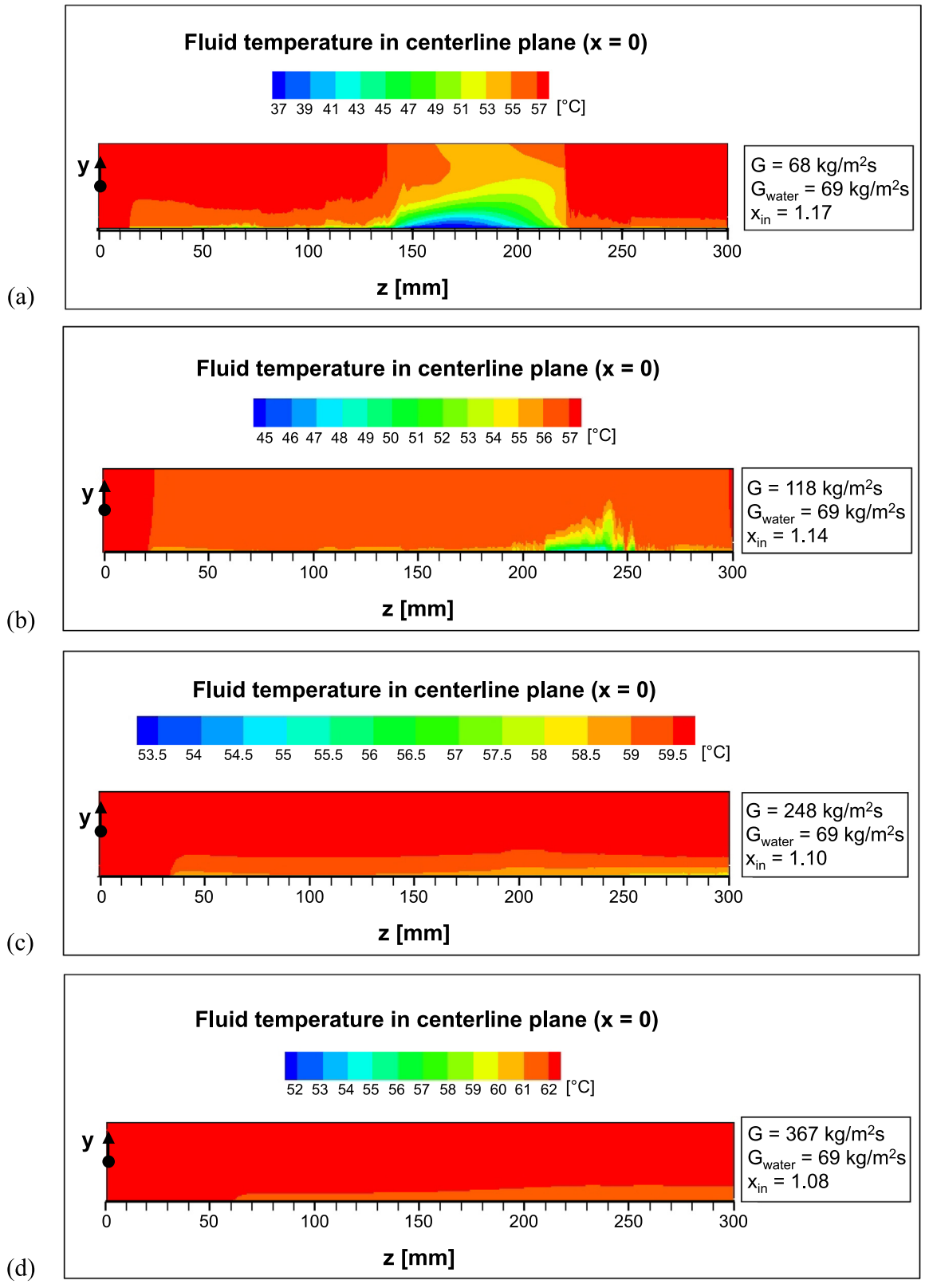

Fig. 16. Contour plots of fluid temperature in centerline plane ($x = 0$) for *Gwater* = 69 kg/m2s and (a) G = 68 kg/m2s, (b) G = 118 kg/m2s, (c) G = 248 kg/m2s, and (d) G = 367 kg/m2s

with the regions of high gradient penetration and full downstream conversion to liquid shifted farther downstream in response to the downstream shift in flow patterns. For $G = 248$ and 367 kg/m^{2}s, Fig. 15(c) and 15(d), respectively, show the upstream fairly uniform gradient covering the entire condensation length because of smooth-annular and wavy-annular flow over the same length, with no significant penetration away from the bottom wall in the absence of slug or bubbly flow patterns.

4.3.3. Comments about parallel channel effects and flow instabilities

A 2003 study by Qu and Mudawar [122] showed how heat sinks containing multiple parallel channels are prone to complex flow instabilities and maldistribution problems. Subsequently, PU-BTPFL investigators performed a series of additional studies on the same phenomena and provided recommendations for their mitigation [10,123–125]. The two most common forms of instability in micro-channel heat sinks are Pressure Drop Oscillation (PDO) and Parallel Channel Instability (PCI). The former takes the form of boundaries between flow patterns oscillating in unison between the inlet and outlet plenums, and results in relatively large pressure drop oscillations. On the other hard, PCI is characterized by relatively mild but random flow pattern fluctuations among the parallel channels, and is associated with relatively mild pressure drop oscillations. As demonstrated by Qu and Mudawar [122], PDO can be mitigated by proper flow control, while PCI can be mostly tolerated. It is important to emphasize that maldistribution of flow among micro-channels can occur even in the absence of instabilities, and result mostly from improper design of upstream and downstream plenums. The issues of both flow instabilities and maldistribution are prevalent in many recent studies on two-phase micro-channel heat sinks (*e.g.,* [126–128]).

Given these prior findings concerning flow instabilities and maldistribution, several strategies are adopted both in terms of design of the test module used in the present study and the flow control. First, the module features enlarged upstream and downstream plenums with flow area over one order of magnitude larger than the total cross-sectional areas of the parallel micro-channels. Each plenum also features a streamlined ramp to ensure both smooth communication with individual channels and equal distribution of flow rate among the channels. In addition, extreme care was exercised when fabricating the individual channels in terms of both tooling and machining. More importantly, while flow patterns do vary slightly among channels, those variations are quite minor as reported in [30,31]. This observation also proves micro-channel condensation modules are far less prone to instabilities than micro-channel boiling modules.

It is for all these reasons that the present flow visualization studies are performed using only one of the two central micro-channels. This also provides a basis for simulating a single channel to model the multi-channel test module, obviously taking advantage of the savings in computing time.

5. Conclusions

This study explored experimentally and computationally flow condensation of FC-72 along a horizontal 1-mm × 1-mm square channel representing a multi-channel cooling module. The channel is cooled along its bottom wall and sidewalls and insulated atop. Wall heat flux is obtained from polynomial curve fits to measured values. The computational portion of the study adopts the VOF method and the Lee interfacial phase change model, which are executed using ANSYS FLUENT. Computed for different operating conditions are dominant time-dependent flow patterns as well as spatial variations of both bottom wall temperature and fluid temperature. Key findings from the study are as following:

(1) The mass transfer intensity factor, γ, in the Lee model has appreciable impact on computational accuracy, with relatively low values producing large deviations from experiment. Good overall agreement is achieved using $\gamma = 33{,}000$ s^{-1}.
(2) The computed flow patterns show good agreement with those captured experimentally using high-speed video. Predicted correctly are dominant smooth-annular, wavy-annular, transition, slug, bubbly, and pure liquid flow patterns, though only a subset of these patterns is prevalent at high FC-72 mass velocities. Also captured computationally for different operating conditions are the expansion and disappearance of injection flow.
(3) A computed flow pattern map, which captures both dominant flow patterns and transition boundaries between flow patterns, matches well a previously developed experimental flow pattern map.
(4) The simulations show good agreement with measured axial variations of bottom wall temperature, evidenced by average deviations ranging from 1.46% to 6.81%. Comparatively larger z-direction gradients are predicted for the lowest mass velocity ($G = 68$ kg/m^{2}s) due to succession of flow patterns occurring over relatively smaller portions of the channel length.
(5) The computational method provides the capability of predicting fluid temperature, which cannot be measured experimentally in a small channel. Detailed spatial variations of fluid temperature are provided both perpendicular to the bottom wall and along the channel. These variations show close correspondence with axial spans of dominant flow patterns. Predicted for the lowest mass velocity ($G = 68$ kg/m^{2}s) are comparatively appreciable temperature changes along the 150-mm upstream portion of the channel as well as the boundary layers along the cooled sidewalls.

Declaration of Competing Interest

NONE The authors declare that they have no known competing financial interests or personal relationships that could have appeared to influence the work reported in this paper.

The authors declare the following financial interests/personal relationships which may be considered as potential competing interests:

Acknowledgements

The authors are grateful for financial support provided by the China Scholarship Council (No. 201806090046) and Scientific Research Foundation of Graduate School of Southeast University (No. YBJJ1804).

Supplementary materials

Supplementary material associated with this article can be found, in the online version, at doi:10.1016/j.ijheatmasstransfer.2019.119158.

References

[1] I. Mudawar, Assessment of high-heat-flux thermal management schemes, IEEE Trans. Compon. Packag. Technol. 24 (2001) 122–141.
[2] I. Mudawar, Two-phase microchannel heat sinks: Theory, applications, and limitations, J. Electronic Packag. 133 (2011) [041002-2].
[3] I. Mudawar, Recent advances in high-flux, two-phase thermal management, J. Therm. Sci. Eng. Appl. 5 (2013) [021012].
[4] H. Zhang, I. Mudawar, M.M. Hasan, Experimental and theoretical study of orientation effects on flow boiling CHF, Int. J. Heat Mass Transfer 45 (2002) 4463–4477.

[5] C. Konishi, I. Mudawar, Review of flow boiling and critical heat flux in microgravity, Int. J. Heat Mass Transfer 80 (2015) 469–493.
[6] I. Mudawar, Flow boiling and flow condensation in reduced gravity, Adv. Heat Transfer 49 (2017) 225–306.
[7] T.M. Anderson, I. Mudawar, Parametric investigation into the effects of pressure, subcooling, surface augmentation and choice of coolant on pool boiling in the design of cooling systems for high-power density chips, J. Electronic Packag. 112 (1990) 375–382.
[8] C.O. Gersey, I. Mudawar, Effects of heater length and orientation on the trigger mechanism for near-saturated flow boiling CHF - I. Photographic and statistical characterization of the near-wall interfacial features, Int. J. Heat Mass Transfer 38 (1995) 629–642.
[9] S. Mukherjee, I. Mudawar, Pumpless loop for narrow channel and micro-channel boiling from vertical surfaces, J. Electronic Packaging 125 (2003) 431–441.
[10] J. Lee, I. Mudawar, Critical heat flux for subcooled flow boiling in micro-channel heat sinks, Int. J. Heat Mass Transfer 52 (2009) 3341–3352.
[11] M.E. Johns, I. Mudawar, An ultra-high power two-phase jet-impingement avionic clamshell module, J. Electronic Packaging 118 (1996) 264–270.
[12] W.P. Klinzing, J.C. Rozzi, I. Mudawar, Film and transition boiling correlations for quenching of hot surfaces with water sprays, J. Heat Treating 9 (1992) 91–103.
[13] M. Visaria, I. Mudawar, Application of two-phase spray cooling for thermal anagement of electronic devices, IEEE Trans. Compon. Packag. Technol. 32 (4) (2009) 784–793.
[14] M.K. Sung, I. Mudawar, Single-phase hybrid micro-channel/micro-jet impingement cooling, Int. J. Heat Mass Transfer 51 (2008) 4342–4352.
[15] M.K. Sung, I. Mudawar, Single-phase and two-phase hybrid cooling schemes for high-heat-flux thermal management of defense electronics, J. Electronic Packaging 131 (2009) [021013].
[16] D.B. Tuckerman, R.F.W. Pease, High-performance heat sinking for VLSI, Electron Device Lett. 2 (1981) 126–129.
[17] C.Y. Yang, R.L. Webb, Friction pressure drop of R-12 in small hydraulic diameter extruded aluminum tubes with and without micro-fins, Int. J. Heat Mass Transfer 39 (1996) 801–809.
[18] Y.Y. Yan, T.F. Lin, Condensation heat transfer and pressure drop of refrigerant R-134a in a small pipe, Int. J. Heat Mass Transfer 42 (1999) 697–708.
[19] H.Y. Wu, P. Cheng, Condensation flow patterns in silicon microchannels, Int. J. Heat Mass Transfer 48 (2005) 2186–2197.
[20] H. Louahlia-Gualous, B. Mecheri, Unsteady steam condensation flow patterns inside a miniature tube, Appl. Therm. Eng. 27 (2007) 1225–1235.
[21] H. Wu, M. Yu, P. Cheng, X. Wu, Injection flow during steam condensation in silicon microchannels, J. Micromech. Microeng. 17 (2007) 1618–1627.
[22] J.S. Hu, C.Y.H. Chao, An experimental study of the fluid flow and heat transfer characteristics in micro-condensers with slug-bubbly flow, Int. J. Refrig. 30 (2007) 1309–1318.
[23] X. Quan, P. Cheng, H. Wu, Transition from annular flow to plug/slug flow in condensation of steam in microchannels, Int. J. Heat Mass Transfer 51 (2008) 707–716.
[24] W. Zhang, J. Xu, J.R. Thome, Periodic bubble emission and appearance of an ordered bubble sequence (train) during condensation in a single microchannel, Int. J. Heat Mass Transfer 51 (2008) 3420–3433.
[25] W. Zhang, J. Xu, G. Liu, Multi-channel effect of condensation flow in a micro triple-channel condenser, Int. J. Multiphase Flow 34 (2008) 1175–1184.
[26] T. Dong, Z. Yang, Measurement and modeling of R141b condensation heat transfer in silicon rectangular microchannels, J. Micromech. Microeng. 18 (2008) [085012].
[27] Y. Chen, R. Wu, M. Shi, J. Wu, G.P. Peterson, Visualization study of steam condensation in triangular microchannels, Int. J. Heat Mass Transfer 52 (2009) 5122–5129.
[28] J. Wu, M. Shi, Y. Chen, X. Li, Visualization study of steam condensation in wide rectangular silicon microchannels, Int. J. Therm. Sci. 49 (2010) 922–930.
[29] X. Ma, X. Fan, Z. Lan, T. Hao, Flow patterns and transition characteristics for steam condensation in silicon microchannels, J. Micromech. Microeng. 21 (2011) [075009].
[30] S.-M. Kim, I. Mudawar, Flow condensation in parallel micro-channels - Part 2: Heat transfer results and correlation technique, Int. J. Heat Mass Transfer 55 (2012) 984–994.
[31] S.-M. Kim, J. Kim, I. Mudawar, Flow condensation in parallel micro-channels - Part 1: Experimental results and assessment of pressure drop correlations, Int. J. Heat Mass Transfer 55 (2012) 971–983.
[32] G. El Achkar, M. Miscevic, P. Lavieille, J. Lluc, J. Hugon, Flow patterns and heat transfer in a square cross-section micro condenser working at low mass flux, Appl. Therm. Eng. 59 (2013) 704–716.
[33] J. Kaew-On, N. Naphattharanun, R. Binmud, S. Wongwises, Condensation heat transfer characteristics of R134a flowing inside mini circular and flattened tubes, Int. J. Heat Mass Transfer 102 (2016) 86–97.
[34] D. Jige, S. Kikuchi, H. Eda, N. Inoue, S. Koyama, Two-phase flow characteristics of R32 in horizontal multiport minichannels: Flow visualization and development of flow regime map, Int. J. Refrig. 95 (2018) 156–164.
[35] H. El Mghari, H. Louahlia-Gualous, Experimental and numerical investigations of local condensation heat transfer in a single square microchannel under variable heat flux, Int. Commun. Heat Mass Transfer 71 (2016) 197–207.
[36] J. Wang, J.M. Li, Y. Hwang, Flow pattern transition during condensation of R134a and R1234ze(E) in microchannel arrays, Appl. Therm. Eng. 115 (2017) 244–255.
[37] G.T. Liang, N. Mascarenhas, I. Mudawar, Analytical and experimental determination of slug flow parameters, pressure drop and heat transfer coefficient in micro-channel condensation, Int. J. Heat Mass Transfer 111 (2017) 1218–1233.
[38] Y. Ding, L. Jia, Study on flow condensation characteristics of refrigerant R410a in a single rectangular micro-channel, Int. J. Heat Mass Transfer 114 (2017) 125–134.
[39] A.H. Al-Zaidi, M.M. Mahmoud, T.G. Karayiannis, Condensation flow patterns and heat transfer in horizontal microchannels, Exp. Therm Fluid Sci. 90 (2018) 153–173.
[40] J. Wang, J.M. Li, Theoretical and experimental study of wavy flow during R134a condensation flow in symmetrically and asymmetrically cooled microchannels, Int. J. Multiphase Flow 101 (2018) 125–136.
[41] R.L. Webb, K. Ermis, Effect of hydraulic diameter on condensation of R-134A in flat, extruded aluminum tubes, J. Enhanced Heat Transfer 8 (2001) 77–90.
[42] S. Koyama, K. Kuwahara, K. Nakashita, K. Yamamoto, An experimental study on condensation of refrigerant R134a in a multi-port extruded tube, Int. J. Refrig. 26 (2003) 425–432.
[43] N.-H. Kim, J.-P. Cho, J.-O. Kim, B. Youn, Condensation heat transfer of R-22 and R-410A in flat aluminum multi-channel tubes with or without micro-fins, Int. J. Refrig. 26 (2003) 830–839.
[44] J.S. Shin, M.H. Kim, An experimental study of condensation heat transfer inside a mini-channel with a new measurement technique, Int. J. Multiphase Flow 30 (2004) 311–325.
[45] X.L. Huai, S. Koyama, An experimental study of carbon dioxide condensation in mini channels, J. Therm. Sci. 13 (2004) 358–365.
[46] A. Cavallini, D. Del Col, L. Doretti, M. Matkovic, L. Rossetto, C. Zilio, Condensation heat transfer and pressure gradient inside multiport minichannels, Heat Transfer Eng 26 (2005) 45–55.
[47] J.S. Shin, M.H. Kim, An experimental study of flow condensation heat transfer inside circular and rectangular mini-channels, Heat Transfer Eng 26 (2005) 36–44.
[48] H. Wu, X. Wu, J. Qu, M. Yu, Condensation heat transfer and flow friction in silicon microchannels, J. Micromech. Microeng. 18 (2008) [115024].
[49] M. Matkovic, A. Cavallini, D. Del Col, L. Rossetto, Experimental study on condensation heat transfer inside a single circular minichannel, Int. J. Heat Mass Transfer 52 (2009) 2311–2323.
[50] C.Y. Park, P. Hrnjak, CO_2 flow condensation heat transfer and pressure drop in multi-port microchannels at low temperatures, Int. J. Refrig. 32 (2009) 1129–1139.
[51] D. Del Col, D. Torresin, A. Cavallini, Heat transfer and pressure drop during condensation of the low GWP refrigerant R1234yf, Int. J. Refrig. 33 (2010) 1307–1318.
[52] H.-K. Oh, C.-H. Son, Condensation heat transfer characteristics of R-22, R-134a and R-410A in a single circular microtube, Exp. Therm Fluid Sci. 35 (2011) 706–716.
[53] J.E. Park, F. Vakili-Farahani, L. Consolini, J.R. Thome, Experimental study on condensation heat transfer in vertical minichannels for new refrigerant R1234ze(E) versus R134a and R236fa, Exp. Therm Fluid Sci. 35 (2011) 442–454.
[54] T. Bohdal, H. Charun, M. Sikora, Comparative investigations of the condensation of R134a and R404A refrigerants in pipe minichannels, Int. J. Heat Mass Transfer 54 (2011) 1963–1974.
[55] H.-Y. Zhang, J.-M. Li, N. Liu, B.-X. Wang, Experimental investigation of condensation heat transfer and pressure drop of R22, R410A and R407C in mini–tubes, Int. J. Heat Mass Transfer 55 (2012) 3522–3532.
[56] M. Derby, H.J. Lee, Y. Peles, M.K. Jensen, Condensation heat transfer in square, triangular, and semi-circular mini-channels, Int. J. Heat Mass Transfer 55 (2012) 187–197.
[57] J. Heo, H. Park, R. Yun, Condensation heat transfer and pressure drop characteristics of CO_2 in a microchannel, Int. J. Refrig. 36 (2013) 1657–1668.
[58] G. Goss, J.C. Passos, Heat transfer during the condensation of R134a inside eight parallel microchannels, Int. J. Heat Mass Transfer 59 (2013) 9–19.
[59] E. Al-Hajri, A.H. Shooshtari, S. Dessiatoun, M.M. Ohadi, Performance characterization of R134a and R245fa in a high aspect ratio microchannel condenser, Int. J. Refrig. 36 (2013) 588–600.
[60] N. Liu, J.M. Li, J. Sun, H.S. Wang, Heat transfer and pressure drop during condensation of R152a in circular and square microchannels, Exp. Therm Fluid Sci. 47 (2013) 60–67.
[61] F. Illan-Gomez, A. Lopez-Belchi, J.R. Garcia-Cascales, F. Vera-Garcia, Experimental two-phase heat transfer coefficient and frictional pressure drop inside mini-channels during condensation with R1234yf and R134a, Int. J. Refrig. 51 (2015) 12–23.
[62] N. Liu, J.M. Li, Experimental study on condensation heat transfer of R32, R152a and R22 in horizontal minichannels, Appl. Therm. Eng. 90 (2015) 763–773.
[63] D. Jige, N. Inoue, S. Koyama, Condensation of refrigerants in a multiport tube with rectangular minichannels, Int. J. Refrig. 67 (2016) 202–213.
[64] N. Liu, H. Xiao, J.M. Li, Experimental investigation of condensation heat transfer and pressure drop of propane, R1234ze(E) and R22 in minichannels, Appl. Therm. Eng. 102 (2016) 63–72.
[65] M.M. Rahman, K. Kariya, A. Miyara, An experimental study and development of new correlation for condensation heat transfer coefficient of refrigerant inside a multiport minichannel with and without fins, Int. J. Heat Mass Transfer 116 (2018) 50–60.
[66] N.H. Kim, Condensation heat transfer and pressure drop of R-410A in flat aluminum multi-port tubes, Heat Mass Transfer 54 (2018) 523–535.

[67] Q. Guo, M.X. Li, H.X. Gu, Condensation heat transfer characteristics of low-GWP refrigerants in a smooth horizontal mini tube, Int. J. Heat Mass Transfer 126 (2018) 26–38.
[68] P. Knipper, D. Bertsche, R. Gneiting, T. Wetzel, Experimental investigation of heat transfer and pressure drop during condensation of R134a in multiport flat tubes, Int. J. Refrig. 98 (2019) 211–221.
[69] K. Sakamatapan, S. Wongwises, Pressure drop during condensation of R134a flowing inside a multiport minichannel, Int. J. Heat Mass Transfer 75 (2014) 31–39.
[70] G. Goss, J.L.G. Oliveira, J.C. Passos, Pressure drop during condensation of R-134a inside parallel microchannels, Int. J. Refrig. 56 (2015) 114–125.
[71] J. Wang, J.M. Li, Pressure drop of R134a and R1234ze(E) during condensation in horizontal microchannel arrays cooled symmetrically and asymmetrically, Exp. Therm Fluid Sci. 96 (2018) 266–283.
[72] W.W.W. Wang, T.D. Radcliff, R.N. Christensen, A condensation heat transfer correlation for millimeter-scale tubing with flow regime transition, Exp. Therm Fluid Sci. 26 (2002) 473–485.
[73] S.M. Kim, I. Mudawar, Universal approach to predicting heat transfer coefficient for condensing mini/micro-channel flow, Int. J. Heat Mass Transfer 56 (2013) 238–250.
[74] S.M. Kim, I. Mudawar, Universal approach to predicting two-phase frictional pressure drop for adiabatic and condensing mini/micro-channel flows, Int. J. Heat Mass Transfer 55 (2012) 3246–3261.
[75] S.M. Kim, I. Mudawar, Review of databases and predictive methods for pressure drop in adiabatic, condensing and boiling mini/micro-channel flows, Int. J. Heat Mass Transfer 77 (2014) 74–97.
[76] H.S. Wang, J.W. Rose, H. Honda, A theoretical model of film condensation in square section horizontal microchannels, Chem. Eng. Res. Des. 82 (2004) 430–434.
[77] H.S. Wang, J.W. Rose, Film condensation in horizontal microchannels: Effect of channel shape, Int. J. Therm. Sci. 45 (2006) 1205–1212.
[78] H.S. Wang, J.W. Rose, Theory of heat transfer during condensation in microchannels, Int. J. Heat Mass Transfer 54 (2011) 2525–2534.
[79] T. Hao, X. Ma, Z. Lan, R. Jiang, X. Fan, Analysis of the transition from laminar annular flow to intermittent flow of steam condensation in noncircular microchannels, Int. J. Heat Mass Transfer 66 (2013) 745–756.
[80] H.S. Wang, J.W. Rose, A theory of film condensation in horizontal noncircular section microchannels, J. Heat Transfer 127 (2005) 1096–1105.
[81] S.-M. Kim, I. Mudawar, Theoretical model for annular flow condensation in rectangular micro-channels, Int. J. Heat Mass Transfer 55 (2012) 958–970.
[82] J. Wu, Y. Chen, M. Shi, P. Fu, G.P. Peterson, Three-dimensional numerical simulation for annular condensation in rectangular microchannels, Nanoscale Microscale Thermophys. Eng. 13 (2009) 13–29.
[83] H. El Mghari, M. Asbik, H. Louahlia-Gualous, I. Voicu, Condensation heat transfer enhancement in a horizontal non-circular microchannel, Appl. Therm. Eng. 64 (2014) 358–370.
[84] J. Wang, J.M. Li, Y. Hwang, Modeling of film condensation flow in oval microchannels, Int. J. Heat Mass Transfer 126 (2018) 1194–1205.
[85] Y. Ding, L. Jia, L. Yin, Y. Zhang, Z. An, Theoretical investigation on convective condensation annular flow of R410a inside rectangular microchannel, Int. J. Heat Mass Transfer 131 (2019) 698–708.
[86] S. Nebuloni, J.R. Thome, Film condensation under normal and microgravity: Effect of channel shape, Microgravity Sci. Technol. 19 (2007) 125–127.
[87] Y. Chen, X. Li, J. Wu, M. Shi, One dimensional numerical simulation for steady annular condensation flow in rectangular microchannels, Heat Mass Transfer 46 (2009) 75–82.
[88] Y. Chen, J. Wu, M. Shi, G.P. Peterson, Numerical simulation for steady annular condensation flow in triangular microchannels, Int. Commun. Heat Mass Transfer 35 (2008) 805–809.
[89] P. Bradshaw, D.H. Ferriss, N.P. Atwell, Calculation of boundary-layer development using the turbulent energy equation, J. Fluid Mech 28 (1967) 593–616.
[90] S. Nebuloni, J.R. Thome, Numerical modeling of laminar annular film condensation for different channel shapes, Int. J. Heat Mass Transfer 53 (2010) 2615–2627.
[91] M.M. Shah, Comprehensive correlations for heat transfer during condensation in conventional and mini/micro channels in all orientations, Int. J. Refrig. 67 (2016) 22–41.
[92] M.M. Shah, A correlation for heat transfer during condensation in horizontal mini/micro channels, Int. J. Refrig. 64 (2016) 187–202.
[93] M.M. Shah, Improved correlation for heat transfer during condensation in conventional and mini/micro channels, Int. J. Refrig. 98 (2019) 222–237.
[94] F.R. Menter, Two-equation eddy-viscosity turbulence models for engineering applications, AIAA J. 32 (1994) 1598–1605.
[95] C.R. Kharangate, I. Mudawar, Review of computational studies on boiling and condensation, Int. J. Heat Mass Transfer 108 (2017) 1164–1196.
[96] E. Da Riva, D. Del Col, Effect of gravity during condensation of R134a in a circular minichannel, Microgravity Sci. Technol. 23 (2011) 87–97.
[97] S. Bortolin, E. Da Riva, D. Del Col, Condensation in a square minichannel: Application of the VOF method, Heat Transfer Eng. 35 (2013) 193–203.
[98] J. Wen, X. Gu, Y. Liu, S. Wang, Y. Li, Effect of surface tension, gravity and turbulence on condensation patterns of R1234ze(E) in horizontal mini/macro-channels, Int. J. Heat Mass Transfer 125 (2018) 153–170.
[99] J. Zhang, W. Li, S.A. Sherif, A numerical study of condensation heat transfer and pressure drop in horizontal round and flattened minichannels, Int. J. Therm. Sci. 106 (2016) 80–93.
[100] X. Gu, J. Wen, C. Wang, X. Zhang, S. Wang, J. Tu, Condensation flow patterns and model assessment for R1234ze(E) in horizontal mini/macro-channels, Int. J. Therm. Sci. 134 (2018) 140–159.
[101] X. Gu, J. Wen, X. Zhang, C. Wang, S. Wang, Effect of tube shape on the condensation patterns of R1234ze(E) in horizontal mini-channels, Int. J. Heat Mass Transfer 131 (2019) 121–139.
[102] S. Chen, Z. Yang, Y. Duan, Y. Chen, D. Wu, Simulation of condensation flow in a rectangular microchannel, Chem. Eng. Process. 76 (2014) 60–69.
[103] H. Ganapathy, A. Shooshtari, K. Choo, S. Dessiatoun, M. Alshehhi, M. Ohadi, Volume of fluid-based numerical modeling of condensation heat transfer and fluid flow characteristics in microchannels, Int. J. Heat Mass Transfer 65 (2013) 62–72.
[104] C. Wu, J. Li, Numerical simulation of flow patterns and the effect on heat flux during R32 condensation in microtube, Int. J. Heat Mass Transfer 121 (2018) 265–274.
[105] D.L. Sun, J. Xu, P. Ding, Numerical research on relationship between flow pattern transition and condensation heat transfer in microchannel, Eng. Comput. 31 (2014) 939–956.
[106] , ANSYS FLUENT 15.0 in Workbench User's Guide, ANSYS Inc, Canonsburg, PA, 2013.
[107] J.U. Brackbill, D.B. Kothe, C. Zemach, A continuum method for modeling surface-tension, J. Comput. Phys. 100 (1992) 335–354.
[108] W. Li, J. Zhang, G. Bai, J.-l. Xu, T.W. Simon, J. Li, J.-j. Wei, Numerical simulation of condensation for R410A in horizontal round and flattened minichannels, J. Heat Transfer 139 (2016) [021501].
[109] W. Li, J. Zhang, P. Mi, J. Zhao, Z. Tao, P.R.N. Childs, T.I.P. Shih, The effect of gravity on R410A condensing flow in horizontal circular tubes, Numerical Heat Transfer, Part A: Appl 71 (2017) 327–340.
[110] F. Gibou, L. Chen, D. Nguyen, S. Banerjee, A level set based sharp interface method for the multiphase incompressible Navier–Stokes equations with phase change, J. Comput. Phys. 222 (2007) 536–555.
[111] R.W. Schrage, A Theoretical Study of Interface Mass Transfer, Columbia University Press, New York, 1953.
[112] I. Tanasawa, Advances in condensation heat transfer, in: Adv. Heat Transfer, 1991, pp. 55-139.
[113] W.H. Lee, Pressure iteration scheme for two-phase flow modeling, in: Multi--Phase Transport: Fundamentals, Reactor Safety, Applications, 1, Hemisphere Publishing, Washington, DC, 1980, pp. 407–431.
[114] GAMBIT, User's Guide, GAMBIT 2.2.30, FLUENT Inc., 2005.
[115] E.W. Lemmon, M.L. Huber, M.O. McLinden, NIST Standard Reference Database 23: Reference Fluid Thermodynamic and Transport Properties-REFPROP, Version 9.0, National Institute of Standards and Technology, Standard Reference Data Program, Gaithersburg, 2010.
[116] J.P. Holman, in: Heat Transfer, 10th ed., McGraw-Hill, New York, 2009, p. 651.
[117] C.R. Kharangate, H. Lee, I. Park, I. Mudawar, Experimental and computational investigation of vertical upflow condensation in a circular tube, Int. J. Heat Mass Transfer 95 (2016) 249–263.
[118] H. Lee, C.R. Kharangate, N. Mascarenhas, I. Park, I. Mudawar, Experimental and computational investigation of vertical downflow condensation, Int. J. Heat Mass Transfer 85 (2015) 865–879.
[119] T.S. Zhao, Q. Liao, Theoretical analysis of film condensation heat transfer inside vertical mini triangular channels, Int. J. Heat Mass Transfer 45 (2002) 2829–2842.
[120] Z.Y. Liu, B. Sunden, J.L. Yuan, VOF modeling and analysis of filmwise condensation between vertical parallel plates, Heat Transfer Res. 43 (2012) 47–68.
[121] J.W. Yu, Y.Q. Jiang, W.H. Cai, F.Z. Li, Forced convective condensation flow and heat transfer characteristics of hydrocarbon mixtures refrigerant in helically coiled tubes, Int. J. Heat Mass Transfer 124 (2018) 646–654.
[122] W. Qu, I. Mudawar, Measurement and prediction of pressure drop in two-phase micro-channel heat sinks, Int. J. Heat Mass Transfer 46 (2003) 2737–2753.
[123] S. Lee, I. Mudawar, Transient characteristics of flow boiling in large micro-channel heat exchangers, Int. J. Heat Mass Transfer 103 (2016) 186–202.
[124] S. Lee, I. Mudawar, Thermal and thermodynamic performance, and pressure oscillations of refrigeration loop employing large micro-channel evaporators, Int. J. Heat Mass Transfer 103 (2016) 1313–1326.
[125] S. Lee, V.S. Devahdhanush, I. Mudawar, Frequency analysis of pressure oscillations in large length-to-diameter two-phase micro-channel heat sinks, Int. J. Heat Mass Transfer 116 (2018) 273–291.
[126] V. Manoj Siva, A. Pattamatta, S.K. Das, Effect of flow maldistribution on the thermal performance of parallel microchannel cooling systems, Int. J. Heat Mass Transf. 73 (2014) 424–428.
[127] R. Kumar, G. Singh, D. Mikielewicz, Numerical study on mitigation of flow maldistribution in parallel microchannel heat sink: channels variable width versus variable height approach, J. Electron. Packag. 141 (2019) 21009–21011.
[128] P. Dąbrowski, M. Klugmann, D. Mikielewicz, Channel blockage and flow maldistribution during unsteady flow in a model microchannel plate heat exchanger, J. Appl. Fluid Mech. 12 (2019) 1023–1035.